Journal of Petroleum Science and Engineering 201 (2021) 108545

Contents lists available at ScienceDirect

Journal of Petroleum Science and Engineering

journal homepage: http://www.elsevier.com/locate/petrol

Pore structure characteristics and evaluation of lacustrine mixed fine-grained sedimentary rocks: A case study of the Lucaogou Formation in the Malang Sag, Santanghu Basin, Western China

Yongshuai Pan [a,b], Zhilong Huang [a,b,*], Tianjun Li [a,b], Xiongfei Xu [c], Xuan Chen [c], Xiaobo Guo [d]

[a] State Key Laboratory of Petroleum Resources and Prospecting, China University of Petroleum (Beijing), Beijng, 102249, China
[b] College of Geosciences, China University of Petroleum (Beijing), Beijing, 102249, China
[c] PetroChina Tuha Oilfield Company, Hami, 839009, China
[d] Xi'an Shiyou University, Xi'an, 710065, China

ARTICLE INFO

Keywords:
Tuffaceous material
Mixed fine-grained sedimentary rock
Pore structure
NMR T_2 spectrum
Fractal dimension

ABSTRACT

The lithology of the mixed fine-grained sedimentary rock reservoirs in the Permian Lucaogou Formation of the Santanghu Basin is very complex, and the reservoirs are dominated by light- and dark-colored laminated structures with extremely heterogeneous pore structure. In this study, the mineral compositions and pore types of the reservoirs were analyzed using thin sections, whole rock X-ray diffraction (XRD), scanning electron microscopy (SEM), and Quantitative Evaluation of Minerals by Scanning Electron Microscopy (QEMSCAN). This analysis was then combined with high-pressure mercury injection (HPMI), water-saturated nuclear magnetic resonance (NMR), and nano-CT scanning to quantitatively characterize the pore structure. In addition, the fractal dimensions obtained by NMR experimentation were used to comprehensively evaluate the pore structure and analyze the effect of volcanic ash on that structure. The results revealed that the reservoirs are characterized by fine-grained (<0.1 mm) minerals of tuffaceous material (felsic minerals) and carbonate, with light-colored lamination containing carbonate minerals and dark-colored lamination containing tuffaceous material. The petrophysical properties of the reservoir were found to be poor, with porosity ranging from 2% to 8% and permeability generally < 0.1 mD. Nanometer scale intergranular pores, intercrystalline pores, vugs, and microfractures are the main reservoir pore types. The NMR T_2 spectra of the dolomite reservoir are mainly characterized by the right unimodal type (1–100 ms), which was mainly caused by the dolomite intercrystal pores and intercrystal dissolution pores, with the larger T_2 components (>100 ms) mostly representing microfractures or vugs. In addition, the HPMI curves display a relatively low entry pressure (3–5 MPa), with medium sorting. The NMR T_2 spectra of the tuff and transitional lithology reservoirs are diverse, however, with the low T_2 components (0.01–1 ms) representing the intracrystal pores, intergranular pores that are mostly blocked by organic matter (OM), and some remaining intergranular pores during compaction, while the right peaks (1–100 ms) are similar to the dolomite reservoir. Also, the HPMI curves exhibit a higher entry pressure (>6 MPa) with poor sorting. Based on the $T_{2cutoff}$ values, the fractal dimensions obtained by the NMR experiment could be divided into two distinct segments, representing different pore structure characteristics. The fractal dimension of the movable fluid pores (D_2) ranged from 2.493 to 2.973 (average 2.765); nevertheless, the fractal dimension of bound fluid pores (D_1) was determined to be unsuitable for fractal theory. Due to the influence of volcanic ash, there is a positive correlation among D_2, felsic mineral content, and TOC, while the D_2 displays a negative correlation with the movable fluid porosity, permeability, and dolomite content. Hence, D_2 increases with increasing felsic mineral content and decreasing dolomite content, indicating that the tuffaceous material can make the pore structure more complex. The relationship between the calcite content and D_2 is not obvious, however, and the clay mineral contents are so low that their effects on the pore structure are negligible. The results of this study indicate that the fractal dimension can comprehensively reflect the pore structure complexity of a mixed fine-grained sedimentary rock reservoir that affected by volcanic ash.

* Corresponding author. State Key Laboratory of Petroleum Resources and Prospecting, China University of Petroleum (Beijing), Beijng, 102249, China.
E-mail address: huangzhilong1962@163.com (Z. Huang).

https://doi.org/10.1016/j.petrol.2021.108545
Received 29 April 2020; Received in revised form 23 October 2020; Accepted 10 February 2021
Available online 13 February 2021

1. Introduction

With the increasing of global demand for oil and gas resources and the declining reserves of conventional oil and gas resources, unconventional resources such as tight oil and gas, shale oil and gas, coalbed methane, and tar sands have gradually attracted people's secondary attention to the petroleum industry (Brandano and Civitelli, 2007; Jarvie, 2010; Lai et al., 2020). As one of the tight reservoirs, the mixed fine-grained sedimentary rock reservoir has made great breakthroughs in recent years. The mixed fine-grained sedimentary rock, which was generally defined as sourcing from several different material types with finer grains (<0.0625 mm), and continuous exploration results at home and abroad have confirmed that it has abundant resource potential (Cózar et al., 2006; Brandano and Civitelli, 2007; Jia et al., 2012; Liu et al., 2015; Zhang et al., 2019). In China, for example, a set of mixed fine-grained sedimentary rocks reservoirs mainly composed of carbonate minerals, clay minerals, and felsic minerals developed in the second member of the Kongdian Formation in the Cangdong Sag. Additionally, the Paleogene Shahejie Formation in the Bohai Bay Basin was found to have developed a set of mixed fine-grained sedimentary rock reservoirs with lacustrine micrite and terrestrial carbonate clastics. Although mixed fine-grained sedimentary rocks have poor petrophysical properties, many exploration wells have obtained industrial oil flow as a result of diagenesis and tectonic modifications (Deng et al., 2019; Fu et al., 2019). In addition, in the Kashan area of the central Iranian Basin, i.e., the Upper Oligocene-Lower Miocene Qom Formation, is a globally unique carbonate stratum containing terrigenous clasts and tephra, which shows good prospects for exploration due to fracture reconstruction (Zhang et al., 2007; Mohammadi et al., 2018). At present, the production of most mixed fine-grained sedimentary rock reservoirs around the world is not stable, however, and the productivity of a single well varies widely, which is mainly related to the heterogeneity of the reservoirs.

Mixed fine-grained sedimentary rock reservoirs are often formed in complex sedimentary environments with complex mineral compositions, thus creating a large number of irregular pores of different scales with complex pore structure (Mount, 1984; McNeill et al., 2012; Fan et al., 2019; Qi et al., 2019). Many scholars have shown that the microscopic pore structure is an important factor affecting reservoir heterogeneity, and they have studied the microscopic pore structure characteristics of tight sandstone, coal, and shale. For example, different pore throat geometries and sizes have different effects on reservoir permeability of tight sandstone (Desbois et al., 2011; Sakhaee-Pour and Bryant, 2014; Zhang et al., 2017; Xi et al., 2016). Effects of different diagenesis on pore types and pore structure of coal and tight sandstone reservoirs (Li et al., 2016; Wang et al., 2020). The characteristics of shale pore structure and the influence of different minerals on its pore structure (Shan et al., 2020; Guan et al., 2020). However, reports on the influencing factors and evaluation of the pore structure of mixed fine-grained sedimentary rocks, especially the more complicated ones with the influence of volcanic ash are still relatively uncommon. Many studies have proved that the storage space of the tight reservoir is characterized by a complex pore network, and the pore structure directly affects the reservoir quality (Li et al., 2016; Shan et al., 2020; Wang et al., 2020). Therefore, it is of great significance to characterize and evaluate the pore structure of mixed fine-grained sedimentary rock reservoirs.

The complex pore structure poses a greater challenge to the traditional evaluation methods, now, there are many methods to learn the mineral composition and pore structure of reservoirs. For instance, the mineral compositions and pore types of the reservoir could be analyzed by means of thin sections, whole rock X-ray diffraction (XRD), scanning electron microscopy (SEM), and Quantitative Evaluation of Minerals by Scanning Electron Microscopy (QEMSCAN) (Giffin et al., 2013; Aboud et al., 2014; Edahbi et al., 2017; Song et al., 2019a,b; Wei et al., 2020). The distribution of pore volume, pore-throat size, pore-body size, and connectivity among pores could be quantitatively or semi-quantitatively characterized by gas adsorption, high-pressure mercury injection (HPMI), nuclear magnetic resonance (NMR), CT scanning, and small-angle neutron scattering (SANS) tests, combined with the corresponding theoretical basis and experimental model (Bai et al., 2013; Clarkson et al., 2013; Zhang and Weller, 2014; Lin et al., 2015; Lai et al., 2015, 2017; Sakhaee-Pour and Bryant, 2015; Zhou and Kang, 2016; Sakhaee-Pour et al., 2017; Shao et al., 2017; Yu et al., 2018; Xu et al., 2020; Wang et al., 2020). However, the principles of various techniques for characterizing pore structure are different and their application scope is also different. (Fig. 1). Therefore, using a single experiment for analysis may produce large errors and inaccuracies. Only when different methods are used to analyze the same sample can the advantages of each one can be better combined, which is also the major advantage of this study.

Firstly proposed by B. Mandelbort in 1975, the fractal theory has been widely used to study the self-similarity of geometric shapes and the structural features of natural objects (Mandelbrot, 1977; Giri et al., 2012; Kulesza and Bramowicz, 2014). Previous researchers have found that the pore structure of rocks was self-similar, and fractal dimension could be used to describe the complexity and regularity of it, which provided an effective means for the evaluation of reservoir pore

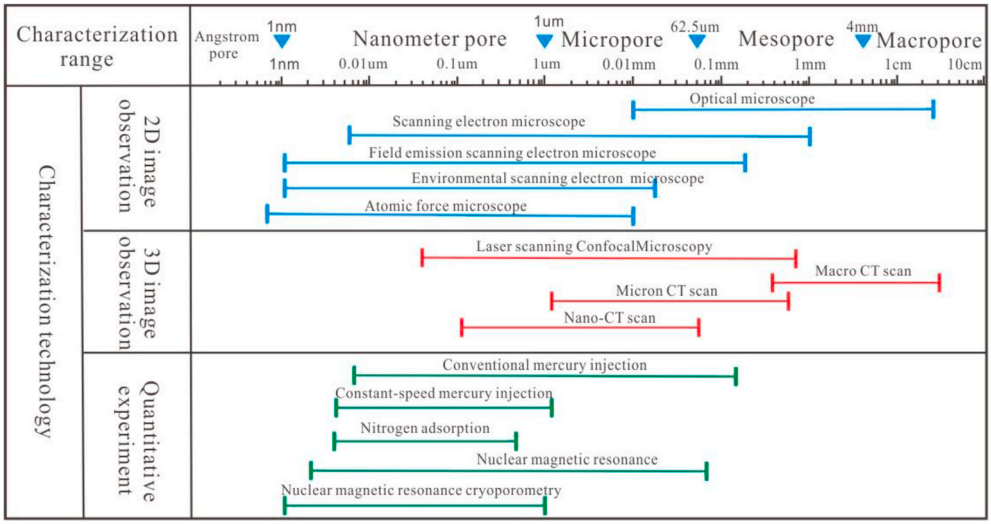

Fig. 1. Application scope of unconventional reservoir pore structure characterization technique (modified from reference Wang et al., 2019).

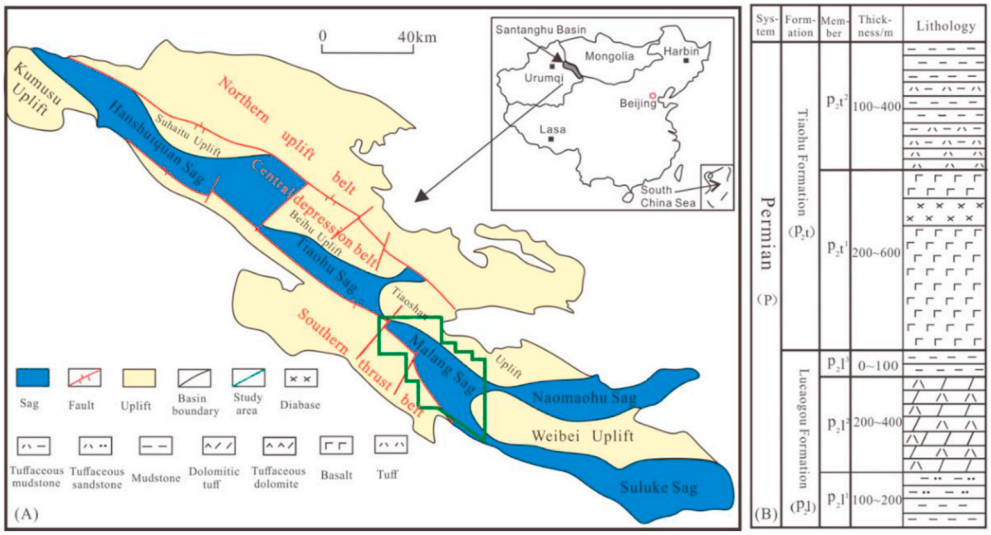

Fig. 2. (A) Location map of the Santanghu Basin, NW China; (B) Regional comprehensive stratigraphic histogram. (modified from reference Liu et al., 2015; Ma et al., 2016).

structure (Katz and Thompson, 1985; Giri et al., 2012; Kulesza and Bramowicz, 2014; Sakhaee-Pour and Li, 2016). In three-dimensional Euclidean space, the fractal dimension ranges from 2.0 to 3.0. The larger the fractal dimension, the rougher the pore surface, and the worse the reservoir quality (Giri et al., 2012; Gao et al., 2014; Lai et al., 2015). In recent years, fractal theory has been widely applied in the field of oil and gas (Gao et al., 2014; Lai et al., 2015; Sakhaee-Pour and Li, 2016; Shao et al., 2017; Fan et al., 2019). Scholars at home and abroad have conducted a lot of fractal analysis on pore structure of tight sandstone, coal, and shale (Gao et al., 2014; Lai et al., 2015; Sakhaee-Pour and Li, 2016; Shao et al., 2017; Fan et al., 2019). For example, Kumar et al. (2019) used N_2 adsorption to study the fractal characteristics of pore structure of shale in Mand-Raigarh Basin, India, and analyzed the organic-inorganic controlling factors of pore structure. Shao et al. (2017) analyzed the pore structure characteristics of tight sandstone and the influence of different mineral types on the fractal dimension by using NMR. Lai et al. (2015) showed the fractal characteristics of large pores and small pores in tight sandstone by applying HPMI, and found that there may be multiple factors in the process of mercury injection that lead to abnormally high fractal dimension of large pores. Liu and Nie (2016) and Zhou et al. (2017) studied the fractal characteristics of coal based on SEM and NMR respectively, and analyzed the effect of fractal dimension on the capacity of methane adsorption. Ma et al. (2019) researched the factors influencing the pore structure of shale by using gas adsorption and NMR fractal dimension. These results have confirmed the great value of the fractal dimension in the characterization and evaluation of pore structure. However, reports on the fractal analysis of mixed fine-grained sedimentary rocks that affected by volcanic ash are still relatively uncommon, and most recent studies mainly focus on mixed siliciclastic-carbonate systems. (Zhao et al., 2017; Fan et al., 2019; Zhang et al., 2019). The Qom Formation in the Iranian Basin is oil producing reservoir in world that contains volcanic ash, however, the percentage of volcanic ash is low (<10%) (Zhang et al., 2007; Mohammadi et al., 2018). Therefore, being able to analyze the effect of volcanic ash on the pore structure is of great significance, especially in mixed fine-grained sedimentary rock reservoirs with high volcanic ash content.

In this study, taking the lacustrine mixed fine-grained sedimentary rock reservoirs affected by volcanic ash in the second member of the Permian Lucaogou Formation (P_2l^2) in the Malang Sag, Santanghu Basin as an example. The mineral compositions and pore structure characteristics are analyzed using casting thin sections, fluorescent thin sections, XRD, cathodoluminescence thin sections, SEM, QEMSCAN, HPMI, NMR, and nano-CT scanning, then the types of storage space and the distribution characteristics of pore throat radius are defined. In addition, the fractal dimensions obtained by NMR experimentation are used to make a more comprehensive quantitative evaluation of the pore structure, and the influence of volcanic ash on the pore structure of mixed fine-grained sedimentary rock reservoirs is researched. Furthermore, the rock types of dominant reservoirs in the study area are identified.

2. Geological setting

The Santanghu Basin, located in the northeastern part of Xinjiang Province of China, is one of a series of small and medium-sized continental petroliferous superimposed basins, bordering the Mongolian Republic in the north, Turpan-Hami Basin to the south, and the Junggar Basin to the west (Fig. 2 A). The Santanghu Basin is sandwiched between the Tianshan and Altai mountains with a long strip distribution from northwest to southeast and covers nearly 2.3×10^4 km^2 area (Liu et al., 2012, 2019; Xu et al., 2013; Ma et al., 2016). Structurally, the Santanghu Basin is located on the collision belt between the Siberian plate and the Kazakhstan plate (Ma et al., 2016; Zhou et al., 2006). In the Early and Middle Permian, the basin was in the stage of regional extension and intracontinental rift, forming numerous high-angled faults and synsedimentary faults. The basin could be divided into three tectonic units: the northern uplift belt, central depression belt, and the southern thrust belt. In addition, the central depression belt could be further divided into 4 uplifts and 5 sags (Zhou et al., 2006; Liu et al., 2012; Ma et al., 2016), of which the Malang Sag was the study area in this study (Fig. 2 A).

There is a lack of Lower Permian, Upper Permian, Upper Triassic, and Upper Cretaceous strata in the Santanghu Basin. The remaining strata are relatively complete, however, and the relationships between most of them are conformable contacts (Liu et al., 2012; Ma et al., 2016). The basin was a lacustrine sedimentary system with frequent volcanic eruptions during the Permian, and the Lucaogou and Tiaohu Formations developed from bottom to top (Liu et al., 2012, 2019; Ma et al., 2016). The key stratum of this study was the P_2l^2 (Fig. 2 B). The volcanic activity during the sedimentary period of the Tiaohu Formation was strong, and a set of huge basalt features approximately 200–600 m thick developed in the first member of the Tiaohu Formation, with diabase intrusions occurring in some areas. Subsequently, the volcanic activity was weak during the second member of the Tiaohu Formation, forming tuff tens of meters thick. By comparison, the volcanic activity was generally weak and frequent during the sedimentary period of the

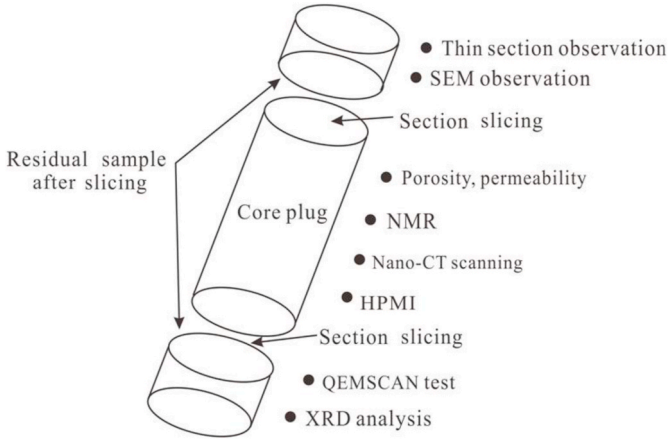

Fig. 3. Experimental scheme for allocating core samples in this study.

Lucaogou Formation, during which a large amount of volcanic ash was deposited, which fell into the lake. This caused the rapid growth of algae and other plankton, resulting in a high abundance of OM (Ma et al., 2016; Liu et al., 2019; Pan et al., 2020). The P_2l^2 was characterized by a hot and arid climate, a suboxic-euxinic condition, a high salt of the lake, a high primary productivity, and a low terrigenous input (Liu et al., 2015, 2019; Ma et al., 2016; Pan et al., 2020). Affected by the frequent volcanic activity around the basin, the P_2l^2 contains a large amount of fine-grained tuffaceous material. Coupled with the arid climate and high salinity conditions, a set of mixed fine-grained sedimentary systems (volcanic ash, carbonate minerals, and terrigenous clastics) developed during the P_2l^2 period (Liu et al., 2015, 2019; Ma et al., 2016; Pan et al., 2020). In addition, influenced by the Indosinian movement, the P_2l^2 in the northeast section of the Malang Sag has been denuded and currently has a small thickness with residual strata mainly distributed in the southwest, and the thickness gradually decreases from southwest to northeast (Liu et al., 2015, 2019; Ma et al., 2016).

3. Experimental samples and methods

3.1. Samples

Forty-two core plug samples in this study were collected from cores of 10 exploration wells in the Malang Sag, Santanghu Basin. On the basis of observing and describing the cores, the samples were collected according to the characteristics of color, structure, microfracture development, tuffaceous material content, and so on. All of the samples were cut parallel to the bedding planes into cylindrical plugs of 3 cm in diameter and 6 cm in length. In order to eliminate the influence of weathering and other factors, all samples were analyzed on a fresh surface. All the experimental samples were prepared according to the scheme in Fig. 3, and the collected plug samples were cut into three parts, of which the middle part was regular plug samples with a height of 3 cm, and the upper and lower ends were residual samples. Generally, the analytical process was divided into two stages, one part is the basic experiments of obtaining underlying parameters of sample by using the residual samples, such as thin sections, XRD, SEM, and QEMSCAN analysis, the other for pore structure characterization by conducting conventional core analysis (porosity, permeability), NMR, nano-CT scanning, and HPMI tests successively using above cut middle part of the sample.

A total of 10 experiments were conducted to analyze the pore structure this time. The exact number of each experiment is as follows, forty-two samples were used for the conventional core analysis (porosity, permeability), casting thin sections, fluorescent thin sections, XRD, cathodoluminescence thin sections, and SEM tests, thirty-one samples were used for water-saturated NMR (twenty-five for fractal analysis) and HPMI experiments, two samples were used for QEMSCAN and nano-CT scanning tests. In addition, more than 100 XRD, thin sections, and SEM data were collected from PetroChina Tuha Oilfield Branch to assist the analysis.

3.2. XRD experimental

The XRD experiment could be used to analyze the mineral composition. Before the experiment, samples need to be crushed in an agate container to a particle size of $<$ 200 mesh (Rietveld, 1969). The instrument used was a D8DISCOVER X-ray diffractometer with working voltage at 30 kV, working current at 10 mA, scanning angle (2θ) at 4.5–50°, and scanning speed at 1°/2θ/min.

3.3. Optical microscopy of thin sections

In this study, three types of thin sections were made, including casting thin sections, fluorescent thin sections as well as cathodoluminescence thin sections, and the production process was all in accordance with the Chinese oil and gas industry standard (Y/T5162-2014). All the thin sections could be used to analyze the mineral composition and pore geometry (Song et al., 2019a,b). The casting thin sections were stained with blue epoxy resin to identify the pore type and size distribution, and a Leica DM4500P/DFC450C high-precision microscope was used for the observation.

The optical microscope used to observe the fluorescent thin sections was the same as that used to observe the casting thin sections, except that a separate luminoscope was added, which could be used in combination with single-polarized and orthogonal light. The view field of the same sample could be obtained under plane polarized light, perpendicular polarized light, and fluorescent light. In addition, fluorescent thin section observation is conducive to analyze the symbiosis of OM with minerals and the effect of OM on pore structure.

The preparation of the cathodoluminescence thin sections requires the sample to be adhered to a standard glass slide with epoxy resin, without the cover glass. The analytical instrument was the CL8200MK5 cathodoluminescence apparatus (with Leica polarizing microscope) of Cambridge instruments, UK with a beam voltage of 12 kA, a beam current of 300 μA, and an exposure time of 1.1 s.

3.4. Porosity and permeability

The porosity and permeability were measured in strict accordance with the Chinese oil and gas industry standard (SY/T 5336-1996), and the instrument used was the ECK-III core permeability tester 08-03-002. The porosity was measured using the helium expansion method, and the relatively stable permeability was determined based on the air flowing through the samples.

3.5. SEM and EDS measurements

SEM is a common electronic imaging technique, which is mainly used to observe the pore structure of rocks at micro/nano scale (Timur et al., 1971; Klaver et al., 2015). This study adopted two methods to observe SEM, one was to use Quanta-200F field emission SEM (with X-ray energy spectrometer) with a minimum resolution of 1.2 nm to observe the pore type, mineral composition, diagenesis, and pore connectivity. The samples were cut into a regular shape before observation, and the conductivity was enhanced by gold-plating the surface of each sample, so as to improve the observation effect. The other one was utilized consisted of cutting the samples into sheets with a length, width, and height of 0.5 cm, 1 cm, and 0.2 mm, respectively, then polishing them with an argon ion beam, and finally plating them with gold to improve their conductivity, which was conducive to observing the pore structure more clearly.

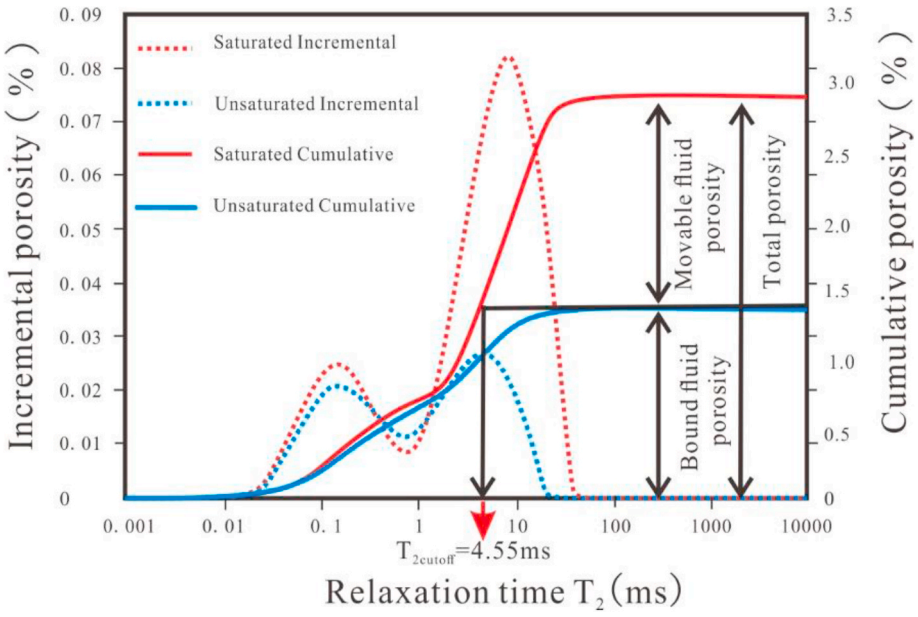

Fig. 4. Schematic diagram of the parameters of water-saturated NMR experiment (modified from reference Shao et al., 2017; Fan et al., 2019).

3.6. HPMI tests

HPMI could provide the distribution of pore throat radius and the connectivity among pores and throats. The instrument used was the kantar PoreMaster-60 full-automatic high-pressure mercury injector, with a maximum mercury injection pressure of 200 MPa, and the radius of the pore throat that could be measured was > 0.004 μm. The principle of HPMI test is to assume that the pores of sample are cylindrical, and the size (radius) of them can be calculated by the Laplace-Washburn equation. In tight reservoirs, pore and throat sizes could differ greatly, so the pore size distribution and pore throat radius measured by HPMI were only relative sizes (Xi et al., 2016; Wang et al., 2020).

3.7. Nano-CT scanning

X-ray nano-scale CT is to use cone X-rays to penetrate an object, then magnify the image through the objective lens of different magnifications, and ultimately reconstruct a three-dimensional stereo model from plentiful X-ray attenuation images obtained by a 360-degree rotation. CT images could reflect the energy attenuation of X-ray during the process of penetrating the object, which could truly reflect the pore structure and the relative density of the core (Nabawy and David, 2016). The testing instrument was a MicroXRM-L200 nm CT scanner with a constant X-ray source voltage of 40 kA and a photon energy of 8 keV. This method is suitable for the analysis of micropores, microfractures, and the connectivity among them (Wang et al., 2020).

3.8. QEMSCAN measurements

QEMSCAN is a technique that combines SEM with EDS to automatically and quickly identify the types and relationships of mineral. QEMSCAN test is capable of scanning the surface of a sample with a high-energy electron beam accelerated along a preset raster scan pattern and producing a color map of the embedded characteristics of the mineral aggregate. The instrument used could emit an X-ray energy spectrum and provide element content information at each measuring point. By combining the grayscale of the back scattered electron (BSE) image with the intensity of the X-ray, the content of the element could be obtained and converted into the mineral facies (Edahbi et al., 2017).

3.9. NMR measurements

Water-saturated NMR test collects the echo attenuation signal of samples after saturated water, and SIRT inversion algorithm is used for mathematical inversion to calculate the T_2 spectrum of samples. The distribution of the NMR T_2 spectrum reflects the pore structure characteristics of rock, and the T_2 relaxation time reflects the chemical environment of the hydrogen protons in a sample, which is related to the binding force and degree of freedom of the hydrogen protons. However, the binding degree of the hydrogen protons is closely related to the internal structure of the sample (Müller-Huber et al., 2016). The T_2 transverse relaxation is more complex because it is caused by three relaxation mechanisms: bulk fluid processes, surface interactions, and diffusion in internal field gradients. However, the reciprocal of the bulk relaxation time and diffusion-induced relaxation time could be ignored. Therefore, T_2 could be directly related to the pore size, as long as the bulk relaxation rate of the pore fluid is known or sufficient to be less than the surface relaxation rate and the diffusion relaxation is minimized (Ge et al., 2014; Müller-Huber et al., 2016; Shao et al., 2017; Lai et al., 2017). The instrument used was a MesoMR23-060-H-I NMR analyzer. In porous media, the larger the pore size, the longer the relaxation time of water, i.e., the location of the peak is related to the size of the pore, and the area size of the peak is related to the number of the corresponding pores (Ge et al., 2014; Shao et al., 2017; Lai et al., 2017). Meanwhile, the parameters such as $T_{2cutoff}$ values, bound fluid porosity, and movable fluid porosity could be obtained based on the incremental and cumulative distribution of T_2 relaxation time (Fig. 4). Movable fluid porosity refers to the percentage of pore volume that could flow in total pore volume, and it directly reflects the permeability of rocks and the connectivity of pores, which could be calculated by comparisons of the T_2 cumulative distribution of water saturated samples and centrifugal samples (Dillinger and Esteban, 2014; Shao et al., 2017). Bound fluid porosity is equivalent to the maximum of unsaturated cumulative curves (Shao et al., 2017). During the experiment, the rock samples were first saturated with 100% brine, and the distribution of incremental and cumulative T_2 relaxation time was recorded. Then, the T_2 relaxation time distribution for each centrifugation process was recorded. Under the irreducible water condition, a horizontal projection line is drawn from the centrifugal cumulative curve, which intersects the saturation cumulative curve to obtain the $T_{2cutoff}$ value (Ge et al., 2014; Lai et al., 2017; Müller-Huber et al., 2016; Shao et al., 2017; Testamanti and

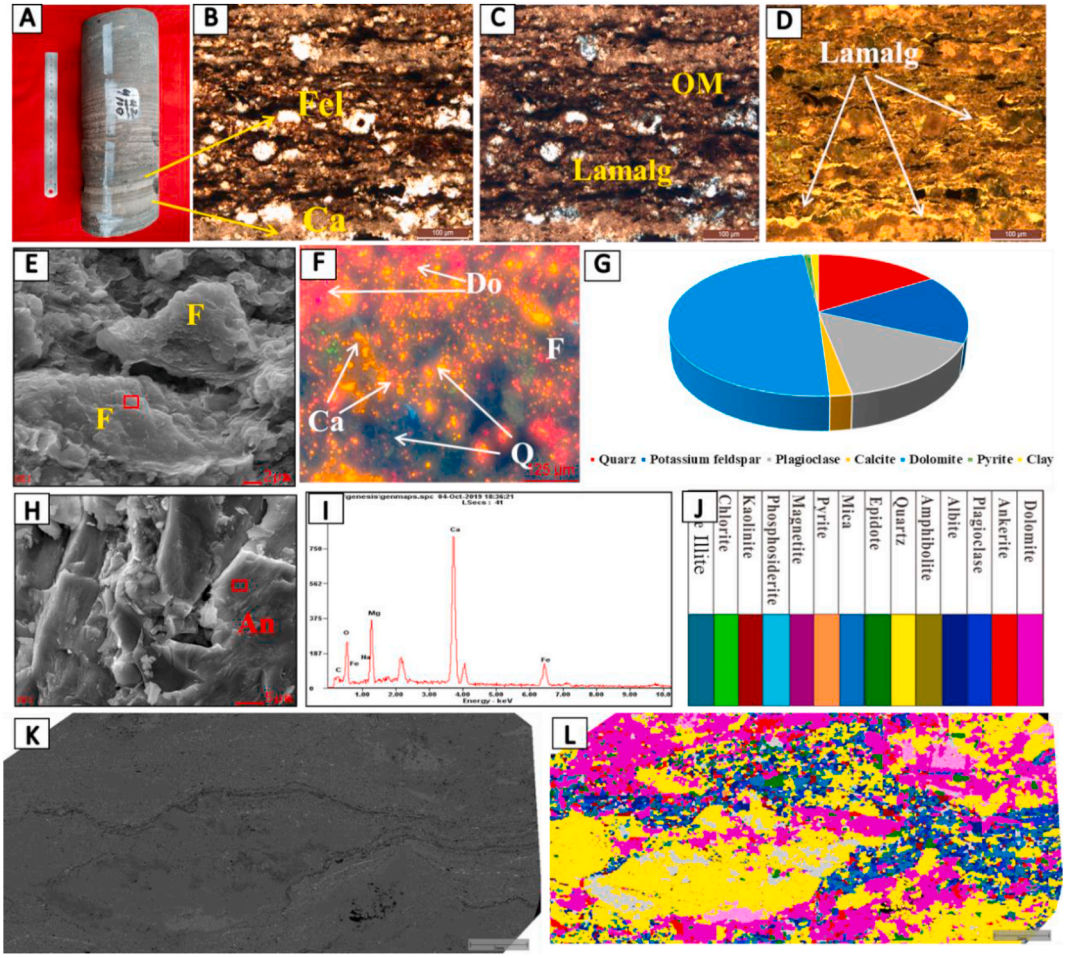

Fig. 5. Analysis chart of mineral types and contents of TD6 sample, well LY1, 3341.63 m. (In this study, each sample was named and numbered according to the lithology. For example, dolomite is named D1, D2, D3, etc., tuffaceous dolomite is named TD1, TD2, TD3, etc., dolomitic tuff is named DT1, DT2, DT3, etc., and tuff is named T1, T2, T3, etc., as shown in Table 1) (A) Core photographs of laminated structures. (B) Laminated fine-grained minerals, plane polarized. (C) The corresponding perpendicular polarized of B. (D) The corresponding fluorescence of B. (E) Feldspar minerals, SEM. (F) Cathodeluminescence photographs, the purple mineral is dolomite, the orange-yellow is calcite, the non-luminous is quartz, and some light blue is feldspar. (G) Pie chart for XRD analysis. (H ~ I) Ankerite minerals, SEM. (J) Legend of QEMSCAN. (K) Back scattered electron image. (L) QEMSCAN mineral analysis map. (Q = quartz; F = feldspar; Do = dolomite; Ca = calcite; OM = organic matter; An = ankerite; Lamalg = lamalginite.). (For interpretation of the references to color in this figure legend, the reader is referred to the Web version of this article.)

Rezaee, 2017; Fan et al., 2019). The $T_{2cutoff}$ value can distinguish the bound fluid and the movable fluid signals, i.e., the T_2 distribution of bound fluid pores is smaller than the $T_{2cutoff}$ value, while the T_2 distribution of movable fluid pores is larger than the $T_{2cutoff}$ value (Lai et al., 2017; Testamanti and Rezaee, 2017).

3.10. Theory of calculating fractal dimension using NMR

Fractal theory has been continuously applied to all walks of life with remarkable results (Mandelbrot, 1977; Giri et al., 2012; Sakhaee-Pour and Li, 2016; Shao et al., 2017; Lai et al., 2017). Because the pore structure of rocks has self-similarity, the fractal dimension could be used to characterize the irregularity and regularity of it (Katz and Thompson, 1985; Giri et al., 2012; Kulesza and Bramowicz, 2014). In the field of oil and gas, fractal methods are increasing and could be divided into two types: direct methods and indirect methods. At present, more indirect fractal methods are used, mainly including HPMI, gas adsorption, NMR, and CT scanning method. Due to the high cost of CT scanning, the other three methods are more commonly used (Li et al., 2015, 2020). This study combined NMR and HPMI to characterize pore structure. Owing to the tight lithology and complex structure in the study area, however, there were fewer macropores, so the amount of mercury injection was lower. In addition, some samples may even generate some microfractures during mercury injection into the pores, which could be confused with pre-existing ones, while other samples may even break completely. As a result, fractal analysis based on HPMI will yield very few data points in large pore segments and multi-segment pore structures, which will bring inaccurate results. In contrast, NMR is an effective, non-destructive, and quantitative method for analyzing the full-scale pore structure of rocks (Shao et al., 2017; Fan et al., 2019). Therefore, the fractal dimension obtained by NMR test was used to evaluate the pore structure this time. Based on the previous research results, the calculation model of fractal dimension of NMR can be expressed as (Li and Horne, 2003; Lai et al., 2017):

$$V_p = \frac{T_2}{T_{2max}}^{3-D} \tag{1}$$

where T_2 is the transverse relaxation time, ms; V_p is the cumulative pore volume fraction, %; T_{2max} is the max transverse relaxation time, ms; D is the fractal dimension.

Take the logarithm transformation of both sides of equation (1) to obtain the calculation equation of fractal dimension in NMR experiment:

$$\log V_p = 3 - D \cdot \log T_2 + (D-3)\cdot\log(T_{2max}) \tag{2}$$

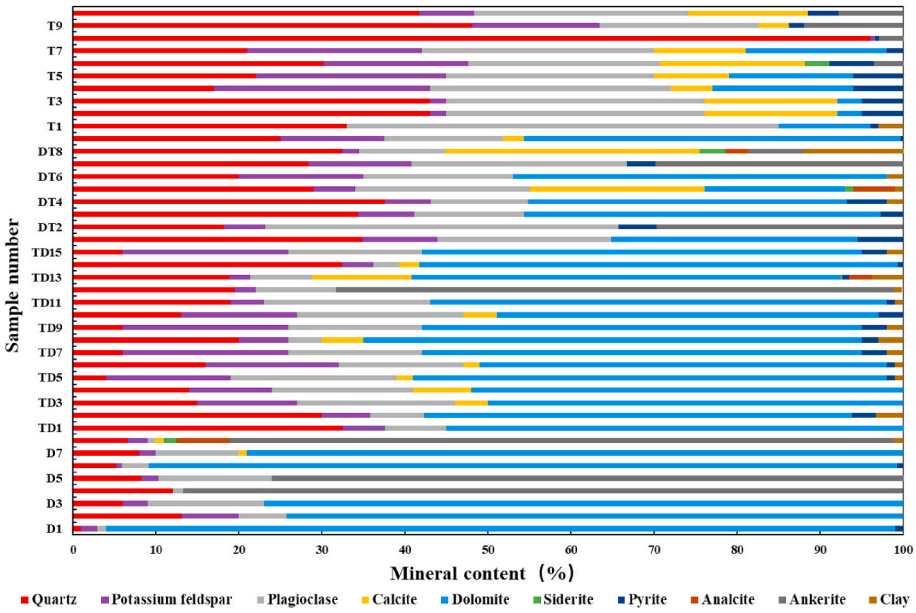

Fig. 6. The XRD mineral composition of 42 samples.

Table 1
Fractal dimensions of all 25 samples derived from NMR measurements (In this study, each sample was named and numbered according to the lithology. For example, dolomite is named D1, D2, D3, etc., tuffaceous dolomite is named TD1, TD2, TD3, etc., dolomitic tuff is named DT1, DT2, DT3, etc., and tuff is named T1, T2, T3, etc.).

Sample	Porosity (%)	Permeability (mD)	Movable fluid porosity (%)	$T_{2cutoff}$ (ms)	$T < T_{2cutoff}$			$T > T_{2cutoff}$		
					K_1	D_1	R^2	K_2	D_2	R^2
D1	10.49	0.030	5.29	11.10	1.866	1.134	0.677	0.507	2.493	0.924
D2	11.01	0.211	3.63	16.64	1.789	1.211	0.650	0.356	2.644	0.936
D3	4.70	0.039	1.40	25.00	1.750	1.250	0.766	0.248	2.752	0.882
TD1	8.12	0.018	1.03	19.56	1.720	1.280	0.655	0.138	2.862	0.977
TD2	4.35	0.011	0.89	0.25	4.929	−1.929	0.837	0.220	2.780	0.908
TD3	8.80	0.038	0.65	77.39	2.939	0.061	0.622	0.057	2.943	0.870
TD4	6.90	0.008	1.30	20.00	2.237	0.763	0.656	0.079	2.921	0.819
TD5	5.00	0.010	0.50	21.00	1.540	1.460	0.824	0.113	2.888	0.951
TD6	5.50	0.021	1.70	22.00	1.567	1.433	0.840	0.207	2.793	0.926
TD7	2.30	0.005	1.00	56.00	1.536	1.464	0.727	0.136	2.864	0.931
TD8	10.00	0.080	3.10	19.00	1.841	1.159	0.889	0.337	2.663	0.921
TD9	4.90	0.019	0.49	52.05	3.191	−0.191	0.644	0.132	2.868	0.903
TD10	7.00	0.004	0.40	64.37	3.017	−0.017	0.625	0.078	2.922	0.885
DT1	2.54	0.010	1.06	4.20	2.335	0.666	0.703	0.173	2.827	0.870
DT2	3.66	0.016	1.88	8.70	1.872	1.128	0.664	0.185	2.816	0.878
DT3	1.41	0.008	0.59	2.38	2.507	0.493	0.688	0.084	2.916	0.936
DT4	2.31	0.063	0.94	0.31	4.425	−1.425	0.832	0.215	2.785	0.914
DT5	1.60	0.005	0.30	80.00	1.221	1.779	0.682	0.027	2.973	0.707
DT6	2.50	0.005	0.22	279.77	2.528	0.472	0.627	0.122	2.878	0.914
T1	2.10	0.004	0.50	30.00	1.690	1.311	0.768	0.067	2.933	0.909
T2	3.40	0.005	1.20	20.00	1.962	1.038	0.809	0.061	2.939	0.811
T3	6.40	0.004	0.90	70.00	1.501	1.499	1.485	0.097	2.903	0.987
T4	0.80	0.065	0.30	7.00	2.140	0.860	0.894	0.079	2.921	0.971
T5	3.20	0.009	0.90	21.00	1.705	1.295	0.854	0.104	2.896	0.868
T6	2.68	0.104	1.24	8.03	2.194	0.806	0.743	0.117	2.883	0.996

Therefore, the fractal dimension D could be obtained based on the slope of the linear with $\log V_p$ and $\log T_2$. For three-dimensional pore space, the fractal dimension generally varies from 2.0 to 3.0. The more complex the pore structure, the higher the fractal dimension (Giri et al., 2012; Gao et al., 2014; Lai et al., 2015). Because the principle of fractal theory has been relatively mature, only the final calculation result of NMR fractal theory is adopted this time, the specific derivation process can refer to previous results (Shao et al., 2017; Lai et al., 2017; Wang et al., 2018).

4. Results

4.1. Mineralogy and petrological characteristics

Geological phenomena of the Santanghu Basin were extremely abundant and the sedimentary environment was very complex. A great number of researches on the sedimentary environment, reservoir properties, geochemical characteristics, and oil enrichment regulation or pattern of the study area have been extensively conducted (Li et al., 2018; Ma et al., 2016; Liu et al., 2019). In general, a set of mixed sediments of carbonate mineral and tuffaceous material developed in the P_2l^2, which was more variable and complex compared with other mixed

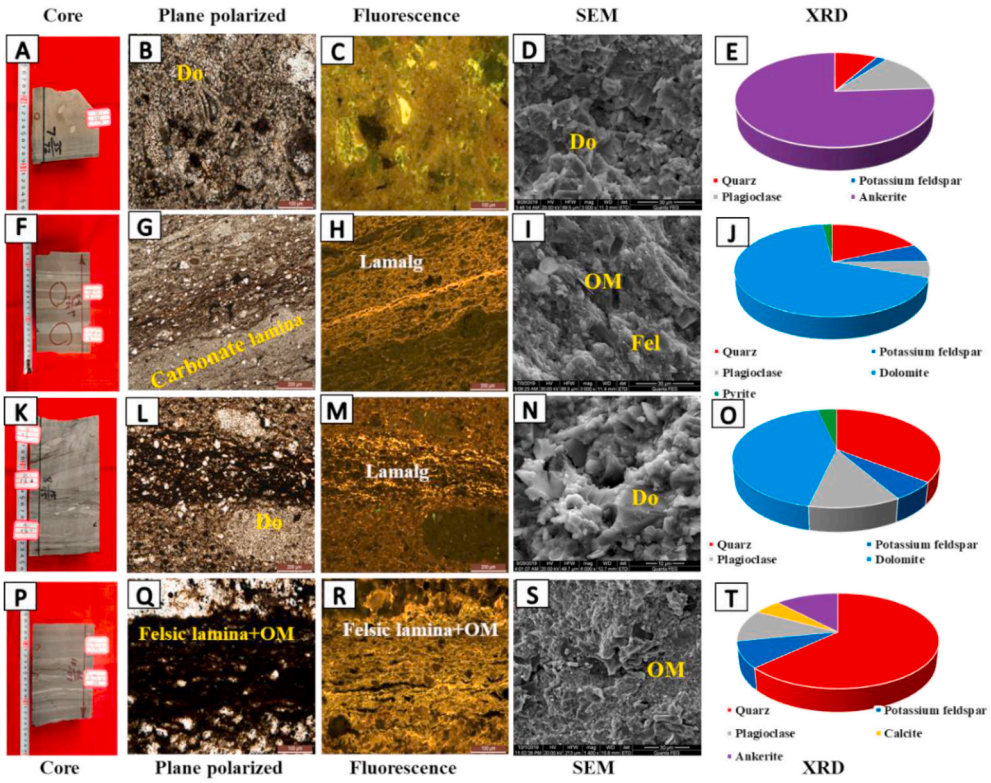

Fig. 7. Core, thin sections, SEM images, and XRD showing mineralogy. (Ã E) Dolomite; well ML1, 3537.6 m. (F ~ J) Tuffaceous dolomite; well L1, 3079.21 m. (K ~ O) Dolomitic tuff; well ML1, 3545.47 m. (P ~ T) Tuff; well L1, 3118.27 m. (Lamalg = lamalginite; Q = quartz; Fel = felsic; Do = dolomite; OM = organic matter.)

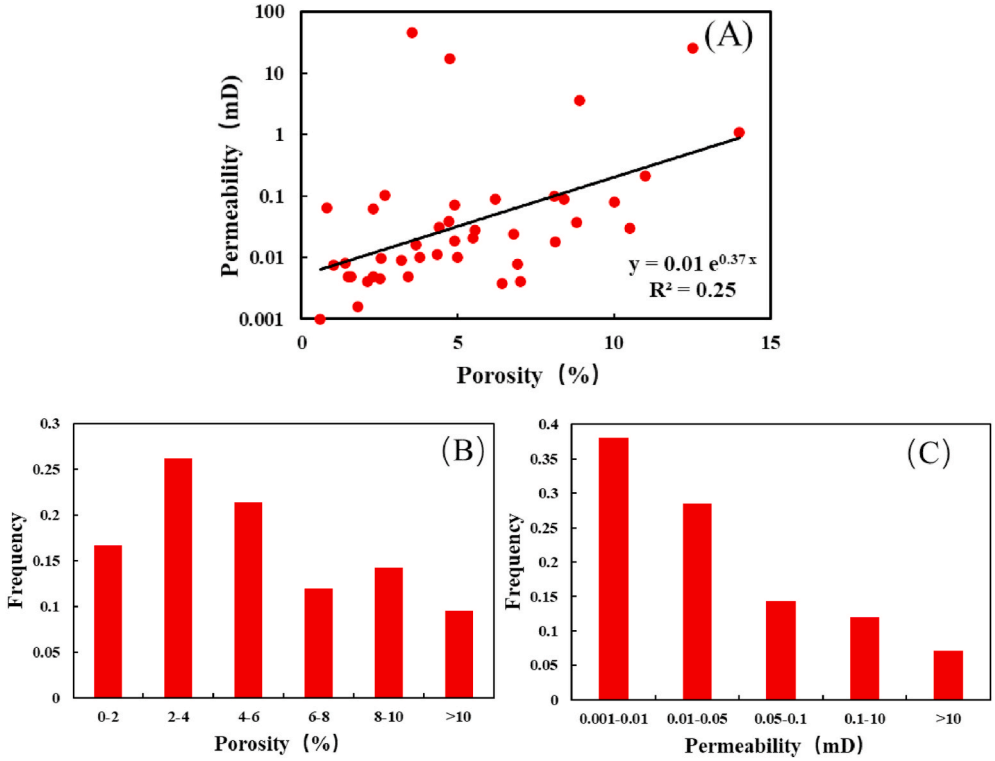

Fig. 8. (A) Cross plot of porosity versus permeability of the 42 samples; (B) Histogram of porosity of the 42 samples; (C) Histogram of permeability of the 42 samples.

sediments. Furthermore, the P_2l^2 revealed special and distinctive characteristic, which was containing a lot of tuffaceous material (the content ranged from 5% to 95%, with an average of approximately 48%), and most of the felsic minerals were formed by devitrification of volcanic glass (Liu et al., 2012, 2019; Ma et al., 2016). Because of the influence of volcanic ash, it was hard to identify the crystal morphology and the type

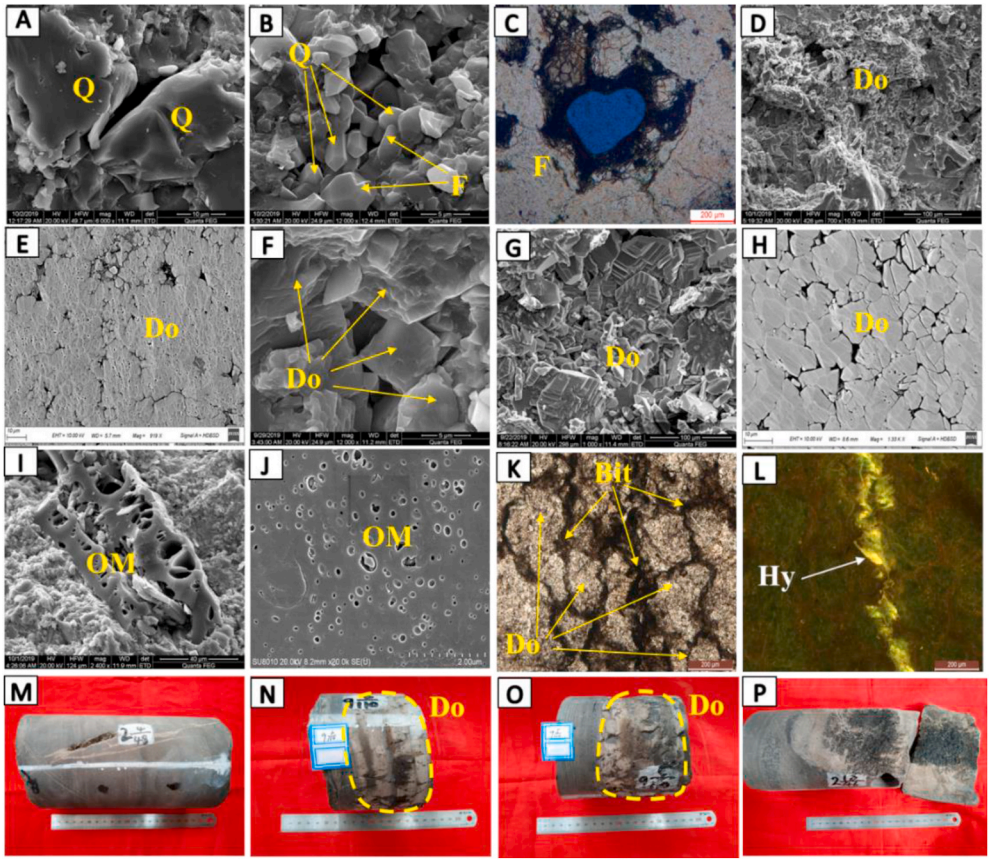

Fig. 9. Thin sections, SEM, and core images showing pore types. (Pores are shown in blue; C and K are casting thin sections; L is fluorescent thin section; M ~ P are core images; The others are SEM and SEM examination of argonion-milled samples.) (Ã B) Intergranular pores of the felsic minerals; A, well L1, 3051.25 m; B, well M708, 2156.51 m. (C) Moldic pores; well M708, 2200.07 m. (D) Dolomite intercrystal dissolution pores; well ML1, 3648.76 m. (E) Intracrystal pores and intracrystal dissolution pores; well LY1, 3305.8 m. (F ~ H) Dolomite intercrystal pores; F, well ML1, 3537.6 m; G, well ML1, 3586.03 m; H, well LY1, 3305.8 m. (I ~ J) OM pores; well ML1, 3595.46 m. (K) Microfractures are filled with bitumen (brown); well M78, 3019 m. (L) Oil-bearing phenomenon in microfractures (pale yellow); well M78, 3019 m. (M) Microfracture is filled with carbonate mineral, which is dissolved later, oil-bearing; well LY1, 3267.16 m. (Ñ O) Microfractures inside the carbonate rocks (light-colored lamination); N, well LY1, 3332.17 m; O, well LY1, 3333.23 m. (P) Oil-bearing phenomenon in microfractures; well M78, 3034.65 m.(Q = quartz; F = feldspar; Do = dolomite; OM = organic matter; Bit = bitumen; Hy = hydrocarbon.). (For interpretation of the references to color in this figure legend, the reader is referred to the Web version of this article.)

of minerals under the ordinary optical microscope. Therefore, comprehensive analysis using various technologies such as thin sections, XRD, SEM, and QEMSCAN revealed that most of the rocks are fine-grained, with sizes of < 0.1 mm (Fig. 5). The specific mineral types are feldspar, quartz, dolomite, calcite, clay, and pyrite (Figs. 5 and 6), but mainly dominated by felsic mineral and dolomite (the total content of them is > 90%), followed by calcite. In addition, the content of clay minerals and pyrite is < 10%, or even not developed, and some samples also contain a small amount of gypsum and other minerals (<5%), indicating that these samples are lacustrine mixed fine-grained sediments (Fig. 6). Most dolomites are ankerites with high OM abundance (Fig. 5H ~ I), which is related to the replacement of Fe^{2+}or Fe^{3+} released by volcanic ash with Mg^{2+} in dolomite (Nishiyama et al., 2001; Li et al., 2014; Rakocinski et al., 2018). The mineral composition of light- and dark-colored lamination is different, with light-colored lamination containing carbonate minerals and dark-colored one containing tuffaceous material. In addition, the abundance of OM in the light-colored lamination is low (Fig. 5Ã D), but that in the dark-colored one is high (Fig. 5Ã D).

Since the total content of felsic and carbonate minerals is > 90%, the rock types of the P_2l^2 could be divided into four categories based on the quantitative analysis results of XRD and the qualitative analysis of thin sections and SEM by taking 70%, 50%, and 25% of the carbonate mineral content (or felsic content) as the limit, i.e., dolomite, tuffaceous dolomite, dolomitic tuff, and tuff. Dolomite is mostly massive structures with many microfractures, and the OM abundance is relatively low (Fig. 7 Ã E). The two types of transitional lithologies, tuffaceous dolomite and dolomitic tuff, are mostly dominated by laminated structures, and as the content of felsic mineral increases, the content of TOC increases accordingly (Fig. 19 A). In addition, a lot of lamalginite that emits orange to yellow fluorescent colors could be seen under the fluorescent microscope (Fig. 7 F ~ O). However, the tuff is mainly dark-colored laminated and massive structure with the highest TOC content (Fig. 7 P ~ T).

4.2. Petrophysical properties

The porosity of the reservoir in the study area was generally found to range from 2% to 8%, with an average of 5.04% (Fig. 8 B), and the horizontal permeability was mostly < 0.1 mD (Fig. 8 C). However, the permeability of some samples varies greatly due to the development of microfractures. There is no significant correlation between porosity and permeability (Fig. 8 A), which is a typical low-porosity and low-permeability reservoir. Combining thin sections and SEM, it is found that the dolomite reservoirs have the best petrophysical properties, followed by tuff, tuffaceous dolomite, and dolomitic tuff reservoirs. The porosity values of tuff, dolomitic tuff, tuffaceous dolomite, and dolomite are 0.8–12.5% (avg. 4%), 1–14% (avg. 3.7%), 0.6–10% (avg. 5.5%), and 4.7–11% (avg. 7.6%), respectively (Table 1). In addition, the tuff, dolomitic tuff, tuffaceous dolomite, and dolomite have permeability values of 0.002–25.9 mD (avg. 4.8 mD), 0.005–1.1 mD (avg. 0.17 mD), 0.001–45.6 mD (avg. 3 mD), and 0.02–3.6 mD (avg. 0.6 mD), respectively (Table 1).

4.3. Pore types of the reservoirs

The primary pores were rarely preserved due to multi-stage diagenetic and tectonic modifications, and abundant secondary pores are formed owing to multiple devitrification process, dolomitization, and dissolution (Choquette and Pray, 1970; Ma et al., 2016; Liu et al., 2019). Using SEM and thin sections, numerous pores were found, mainly consisting of intergranular pores, intercrystal pores, intracrystal pores, intergranular dissolution pores, intercrystal dissolution pores, vugs, microfractures, and OM pores.

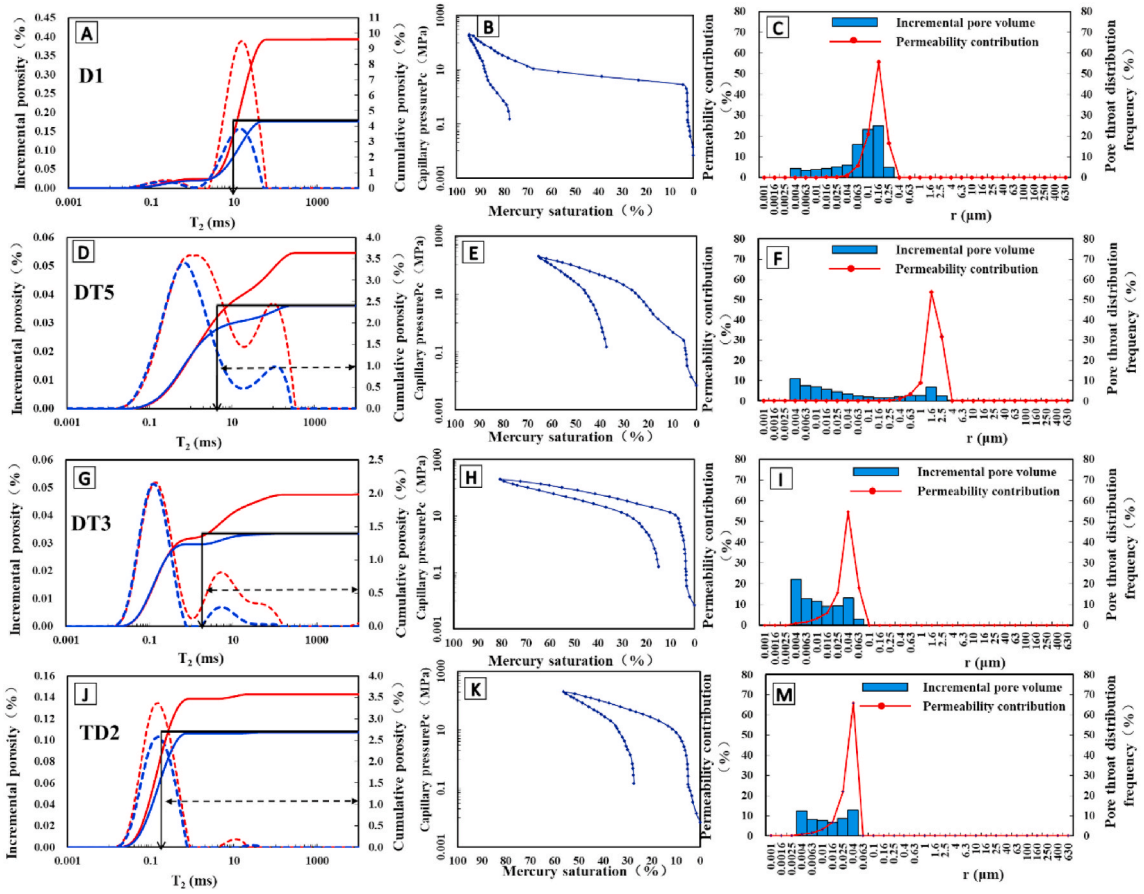

Fig. 10. Pore structures of samples D1, TD2, DT3, and DT5 were characterized by NMR and HPMI. (Ã C) Dolomite; D1, well M62, 2880 m. (D ~ F) Tuff; DT5, well M78, 3043.1 m. (G ~ I) Dolomitic tuff; DT3, well ML1, 3543.8 m; (J ~ M) Tuffaceous dolomite; TD2, well M62, 3590.43 m.

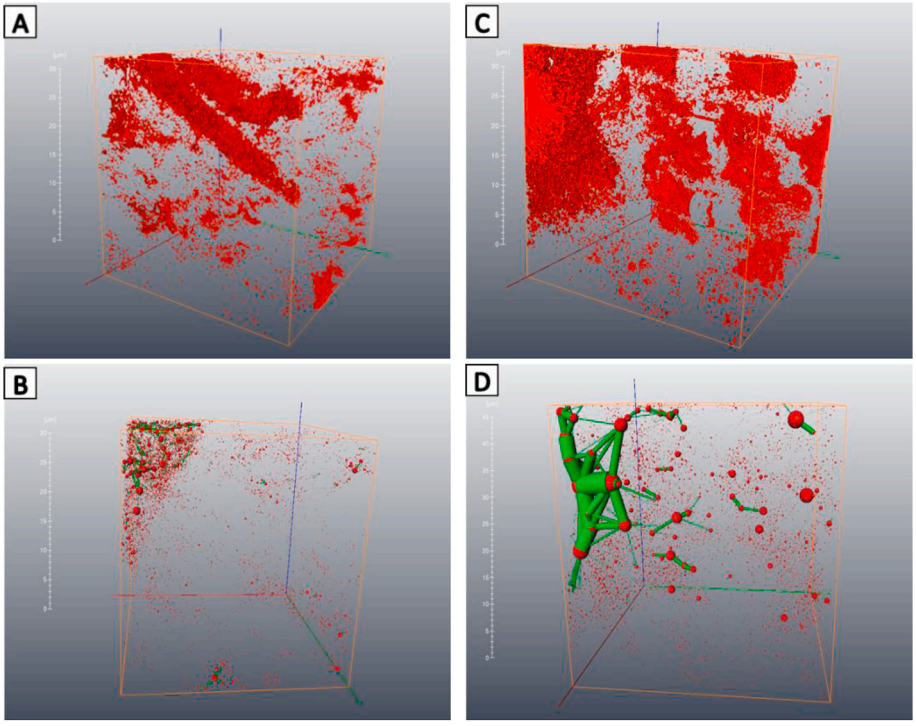

Fig. 11. Characteristics of pore structure in nano-CT scanning. (Ã B) T7, well LY1, 3334.4 m. (C ~ D) TD11, well LY1, 3297.5 m.

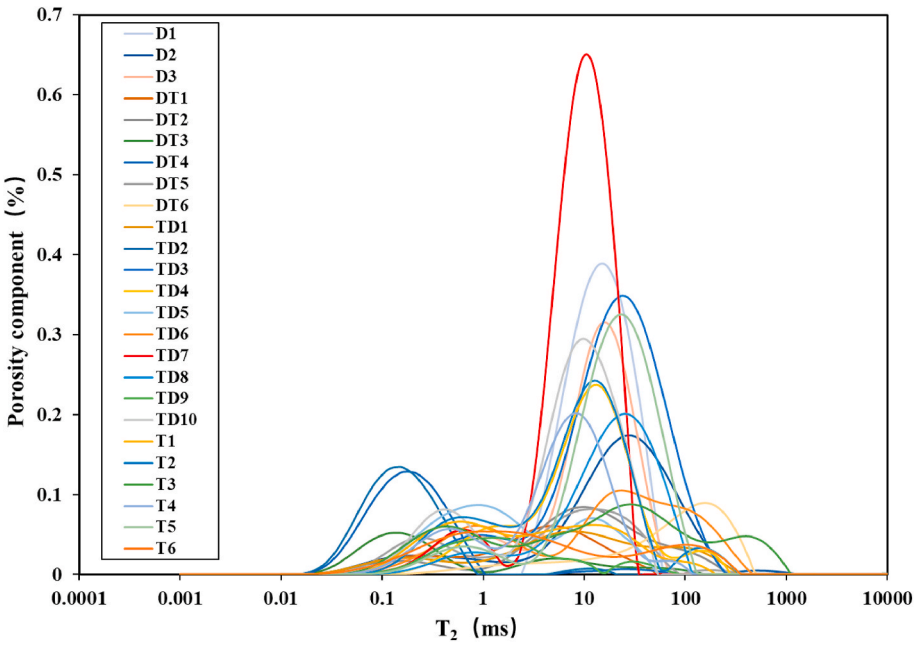

Fig. 12. NMR T_2 relaxation time distribution of 25 samples.

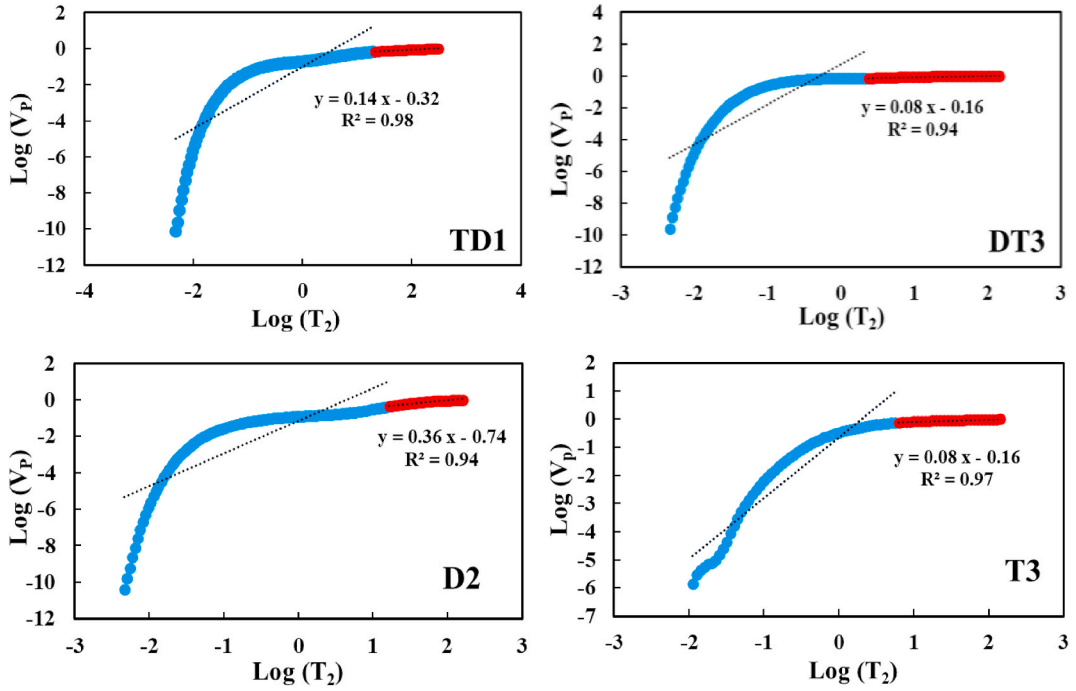

Fig. 13. Plots of log (V_p) versus log (T_2) using NMR: TD1, well L1, 3078.8 m; DT3, well ML1, 3543.8 m; D2, well ML1, 3638.6 m; T3, well LY1, 3271.46 m.

Casting thin sections and SEM images revealed that the intergranular pores with a scale of nanometer, were scattered between the felsic particles, and the pore radius mainly ranged from 0.001 μm to 2 μm. Most of the intergranular pores were either plate-like and column-like in shape, with fewer large pores and throats (Fig. 9 A, B). However, the dissolution enlarged intergranular pores improved the pore systems of the P_2l^2 tuff reservoirs (Fig. 9 C).

Intercrystal and intracrystal pores were the main pore types that developed in the dolomite reservoirs, which would even become larger and more irregular due to dissolution, with diameters ranging from a few microns to hundreds of microns (mainly range from 0.01 μm to 4 μm) (Fig. 9 D ~ H). Although the pore size of intercrystal pores was small, they were numerous and played an important role in improving the petrophysical properties of reservoirs under the transformation of dissolution (Fig. 9 D ~ H). In addition, some carbonate or felsic minerals may even be significantly dissolved to form moldic pores and open vugs (Fig. 9 C, D).

OM pores refer to the pores generated by OM during the hydrocarbon generation process due to the reduction of OM volume, and have a greater relationship with maturity. When the maturity of OM is higher, the number of OM pores is much higher. However, when the maturity is low, the number of OM pores is small, and most are not connected. Hence, they contribute little to the petrophysical properties of reservoirs (Song et al., 2019a,b). The vitrinite reflectance (R_o) values of the P_2l^2

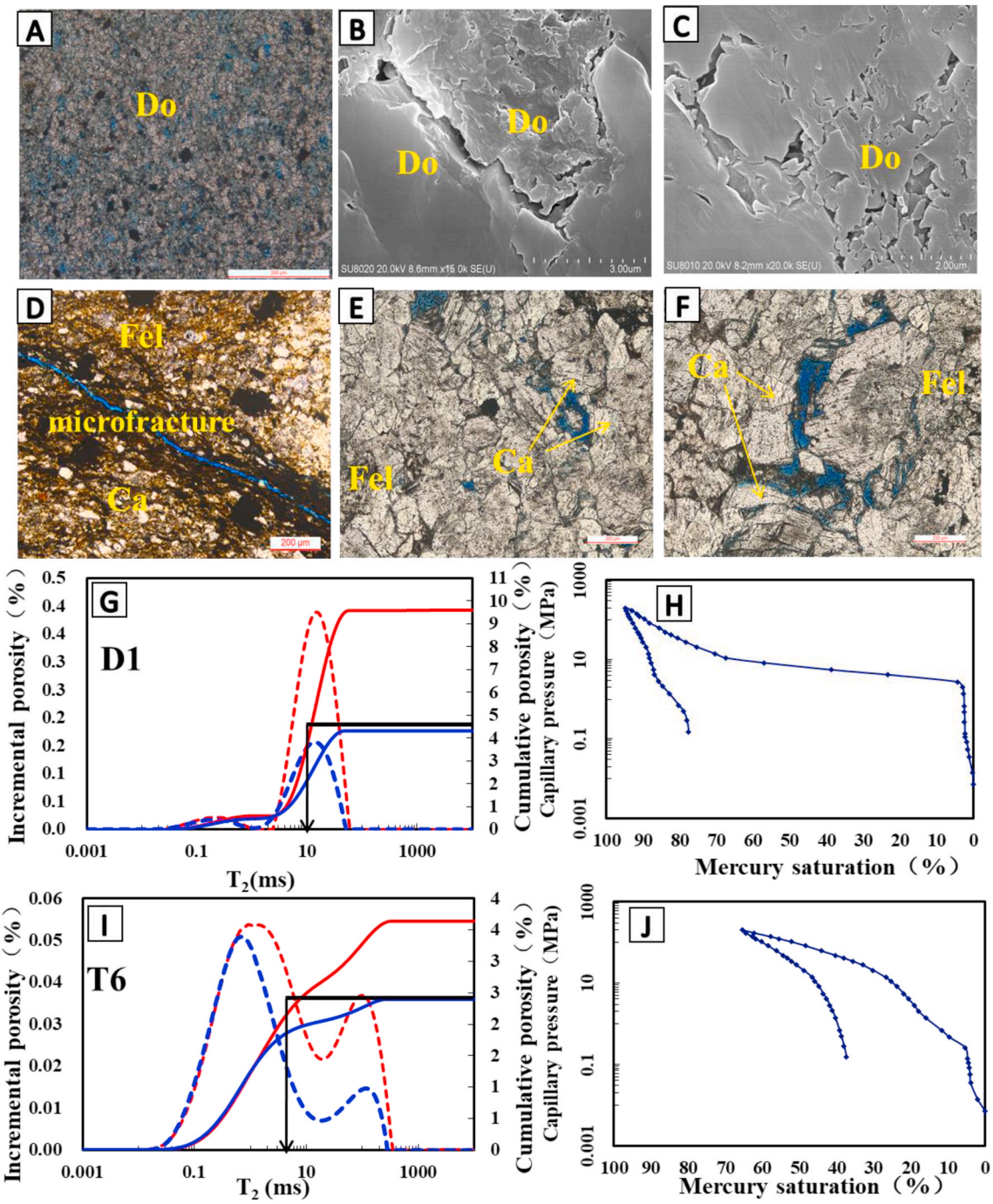

Fig. 14. Pore structure characteristics of samples D1 and T6. (Ã C) Dolomite intercrystal pores and intercrystal dissolution pores; D1, well M62, 2880 m. (D ~ F) Microfractures and vugs; T6, well M78, 3043.1 m. (G) NMR T_2 relaxation time distribution of D1. (H) HPMI curve of D1. (I) NMR T_2 relaxation time distribution of T6. (J) HPMI curve of T6. (Do = dolomite; Ca = carbonate; Fel = felsic.)

ranged from 0.5% to 0.9% (Liu et al., 2017), so, the OM pores were poorly-developed with poor connectivity. The OM pores had diameters < 0.1 μm wide and were mainly isolated round, oval, and irregular in shape according to the SEM observed results (Fig. 9 I ~ J). In addition, the percentage of the OM pores was very small (<5%), and such pores were relatively well developed in tuff reservoirs.

Structure fractures refer to the fractures that are caused by tectonic stress, which could cut through many mineral particles and connect some intergranular pores. Some fractures may be dissolved later, resulting in a further increase in width and more irregular edges, which could also connect more pores and fractures (Liu et al., 2019; Lai et al., 2020). The width of microfractures could be from a few microns to a few millimeters, which could greatly improve the storage and seepage capacity of the reservoir (Liu et al., 2019; Lai et al., 2020). Core observation and thin sections identification revealed that there were quite a few irregular microfractures in this study area (Fig. 9 K ~ P), which were partially filled with calcite and dolomite (Fig. 9 M). However, the unfilled and dissolved microfractures could show obvious oil-bearing phenomenon (Fig. 9 K ~ P), and the width of them was usually < 50 μm. Most of the microfractures were developed in the dolomite reservoirs, it could be clearly seen on the core that the microfractures inside the carbonate rocks (light-colored lamination) were restricted by the tuff

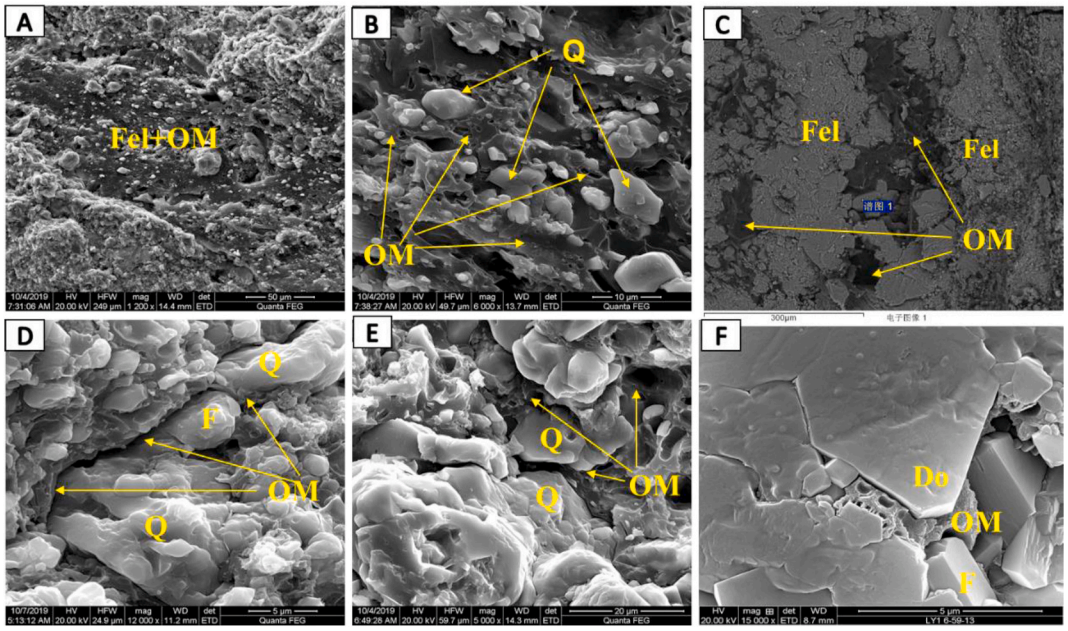

Fig. 15. SEM images showing the pores are blocked with OM. (Ã B) Laminated OM blocks the intergranular pores of felsic minerals; well L1, 3095.61 m. (C ~ E) OM blocks the intergranular pores of felsic minerals; C, D, well ML1, 3550.3 m; E, well L1, 3128.93 m. (F) Intercrystal pores of dolomite crystals are blocked with OM; well LY1, 3297.93 m.(Q = quartz; F = feldspar; Do = dolomite; OM = organic matter; Fel = felsic.)

(dark-colored lamination) at the upper and lower ends (Fig. 9 Ñ O).

4.4. Pore structure characteristics

The pore structures of the reservoirs in the P_2l^2 are very complex, exhibiting four main types of NMR T_2 spectra, and HPMI curves that generally display narrow plateaus with skewness large slanting degrees (Fig. 10). Dolomite reservoir, as an important reservoir, the T_2 spectra of it were characterized by an obvious right unimodal type and a long relaxation time. Generally, the T_2 relaxation time of the major peak is located beyond 10 ms, i.e., the distribution of large pores is predominant (Fig. 10 A). The plateaus of the HPMI curves are relatively broad with a smaller slanting degree and good sorting, indicating that the large throats are widely distributed. The entry pressure is 5 MPa on average, and the pore throat radius is approximately 0.16 μm (Fig. 10 B, C).

Tuff, tuffaceous dolomite, and dolomitic tuff reservoirs have more complex pore structures with a variety of T_2 spectra, including the bimodal type with large and small pores (Fig. 10 D), the left unimodal type dominated by small pores (Fig. 10 G ~ J), and the right unimodal type characterized by large pores. For HPMI, the capillary pressure curves of most samples have no obvious plateaus, with skewness with larger slanting degrees, and poor sorting. Furthermore, the HPMI curves have a higher entry pressure, which is generally > 6 MPa (Fig. 10 E, H, K), and the pore throat radius mainly range from 0.004 μm to 0.1 μm (Fig. 10 F, I, M). However, the radius of some microfracture are significantly abnormal (Fig. 10 F). In addition, nano-CT scanning reveals uneven distribution of pores with poor connectivity, small pore throat radius, and strong heterogeneity (Fig. 11).

4.5. Fractal analysis from NMR

The NMR T_2 spectra are similar among different samples, which cannot accurately distinguish the difference of pore structure (Fig. 12). According to the NMR experiment results and fractal theory, there is an obvious linear relationship between the T_2 relaxation time and the cumulative pore volume (V_p) on a log-log plot. The V_p and T_2 relaxation time of each sample calculated based on equation (2) were plotted on a logarithmic scale and it was found that the curve had a clear two-segment characteristics (Fig. 13). Based on Eqs. (1) and (2), the fractal dimensions of the first segments ($T_2 < T_{2cutoff}$) recorded as D_1 (bound fluid pores) are < 2, and the second segments ($T_2 > T_{2cutoff}$) recorded as D_2 (movable fluid pores) range from 2.493 to 2.973 (avg. 2.842) (Table 1). The correlation coefficient of D_2 ranging from 0.707 to 0.996 with an average of 0.904, is higher than that of D_1 varying from 0.622 to 0.894 with a mean value of 0.737 (Table 1), indicating that the fractal theory is more applicable for the large pores (movable fluid pores).

5. Discussions

5.1. Influence factors of different pore structure characteristics

Complicated sedimentary environment, multi-stage diagenesis, and tectonic activities often lead to reservoirs with complicated rock types and pore networks, resulting in extreme heterogeneity of the pore structure (Lai et al., 2020). During the sedimentary period of the P_2l^2, a large amount of fine-grained tuffaceous material was deposited in the study area under the influence of frequent volcanic activity around the basin, which promoted the bloom of algae and resulted in a high abundance of OM.

Different peaks of the NMR T_2 spectra represent different pore size ranges of rocks (Shao et al., 2017; Wang et al., 2018). The pore structure of conventional reservoirs could often be distinguished based on peak types of the T_2 spectra, while the peak types of tight reservoirs are more complicated. T_2 spectra of the reservoir in the study area have four types (Fig. 10), and the types of different lithologies are different, which means that different lithologies have different pore structures. If the pore size corresponding to different pore types of tight reservoirs could be accurately identified, it would have certain practical significance for improving the recovery of mixed fine-grained sedimentary rock reservoirs. In this study, HPMI experiment was used to accurately obtain a coefficient (surface relaxation) to convert the NMR T_2 relaxation time (ms) into the pore radius (um) (Li et al., 2015, 2020). The combination of casting thin sections and SEM revealed that the right unimodal type of the T_2 spectra of the dolomite reservoir (1 ms < T_2 < 100 ms) mainly represents dolomite intercrystal pores and intercrystal dissolution pores (pore radius varies from 0.16 μm to 1.6 μm) (Fig. 14 Ã C, G). Although

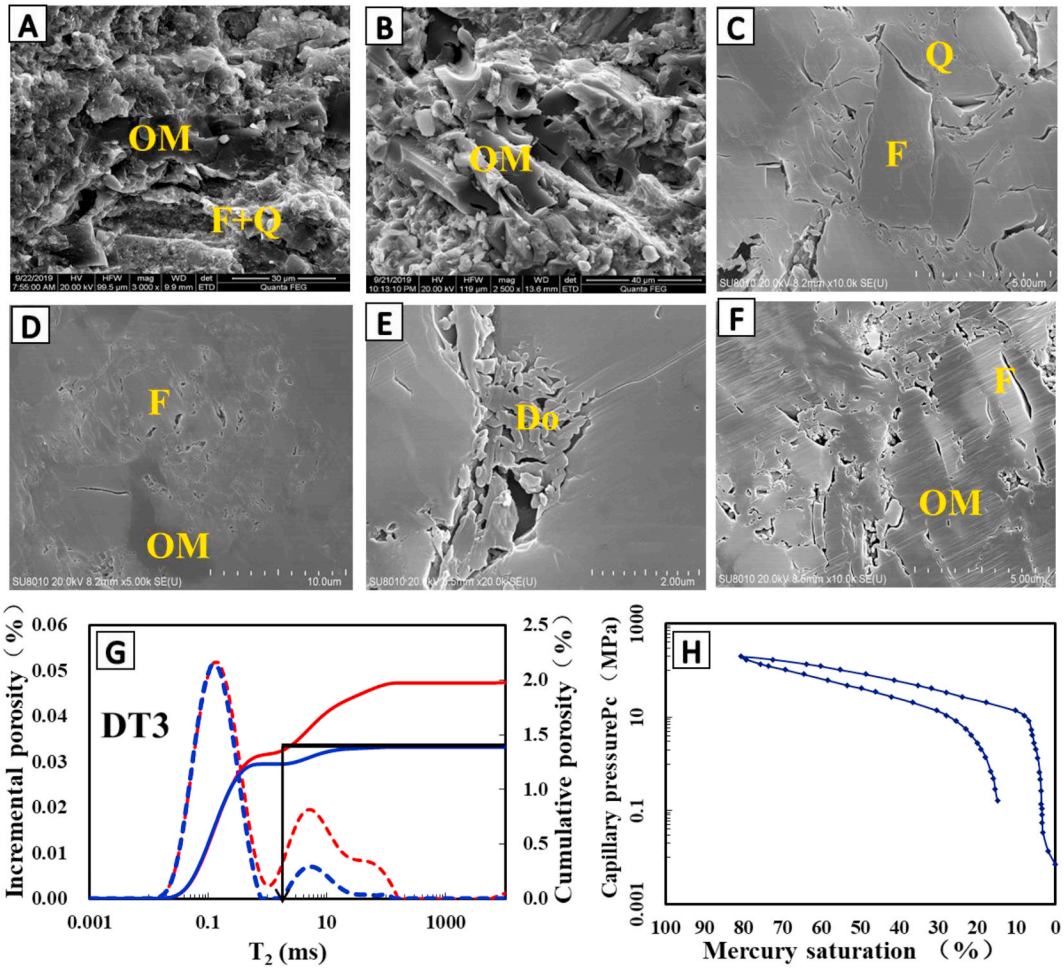

Fig. 16. Pore structure characteristics of sample DT3; well ML1, 3543.8 m. (Ã B) Intergranular pores are blocked with OM. (C ~ D) Intergranular pores of felsic minerals. (E) Intercrystal pores. (F) Intergranular pores and partial intergranular dissolution pores. (G) NMR T_2 relaxation time distribution. (F) HPMI curve. (Q = quartz; F = feldspar; Do = dolomite; OM = organic matter.)

the primary pores of the ancient dolomites are less preserved, abundant secondary pores could be formed due to dolomitization and burial dissolution. The pore diameters of these secondary pores range from several hundred nanometers to several micrometers, and even some dissolution fractures could have a radius of several centimeters, which greatly improves the petrophysical properties of the reservoir (Lai et al., 2020). This is also the reason that the slanting degree of the HPMI curve of the dolomite reservoir is relatively small, and the entry pressure is relatively low (Fig. 14 H). Part of the T_2 components is larger (100–1000 ms) (Fig. 14 I) due to the development of microfractures and vugs with better connectivity, resulting in significant differences in T_2 relaxation time and $T_{2cutoff}$ values from normal pores (Fig. 14 D ~ F, J). With the help of HPMI analysis, the proportion of large pores (>100 nm) of the dolomite reservoirs was found to exceed 60% (Fig. 10 C), and the contribution to reservoir permeability can reach more than 70% (Fig. 10 C).

The pore structures of the transitional lithologies and tuff reservoirs are more complicated, and the T_2 spectra and HPMI curves are also complex and diverse, with very poor regularity (Fig. 10 D ~ M). During the sedimentary period of the P_2l^2, the Santanghu Basin was affected by a large amount of tuffaceous material from the periphery of the basin, which led to an algal bloom, thus resulting in a high abundance of OM, especially tuff, with a higher content of OM (Fig. 7 P ~ T). SEM images, however, showed that a large amount of algal OM would block the intergranular pores of the feldspar minerals symbiotic with the OM (Fig. 15). Moreover, due to the OM pores were poorly-developed in these samples, the complexity of pore structure was greatly increased and the porosity of rocks was greatly reduced. The left peak of the NMR T_2 spectra (0.01 ms < T_2 < 1 ms) mostly represents the intracrystal pores with a small radius and intergranular pores partially blocked by OM (Fig. 16 Ã B, G ~ H), as well as some intergranular pores remaining after compaction (pore radius is < 0.1 μm or even smaller) (Fig. 16 C ~ D). The right peak (1 ms < T_2 < 100 ms) is similar to the dolomite reservoir, mainly representing the dolomite intercrystal pores and intercrystal dissolution pores (Fig. 16 E ~ F), since the influence of volcanic ash on the dolomite was relatively small.

The type, size, geometry, and connectivity of the pores control the fluid flow capacity in reservoir (Fan et al., 2019; Lai et al., 2020). Pores with poor connectivity (intracrystal pores and intergranular pores partially blocked by OM) usually correspond to the low T_2 components (1–100 ms). Interconnected pores (intergranular pores, intercrystal pores, intergranular dissolution pores, and intercrystal dissolution pores) usually refer to the moderate T_2 components (1–100 ms), while some of the vugs and microfractures correspond to the larger T_2 components (100–1000 ms). Microfractures are considered to be an important contributor to the pore network. In some cases, the microfractures could be interconnected with intergranular pores, intercrystal pores, and their dissolution pores, thereby significantly improving permeability (Fig. 17).

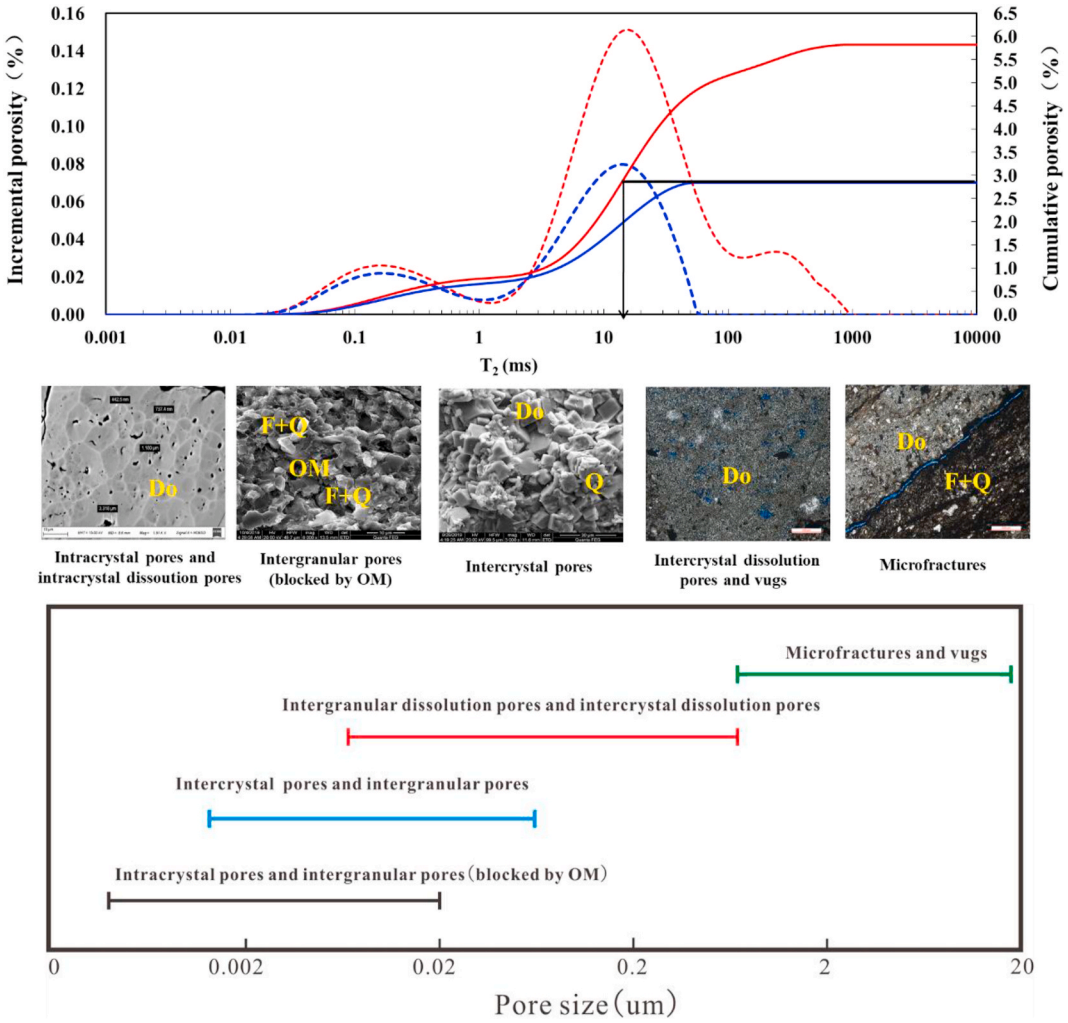

Fig. 17. NMR, thin section, SEM, and HPMI showing the pore network spectrum of the P_2l^2 in Santanghu Basin (The quantitative classification of pore size distribution was obtained according to the joint test of NMR and HPMI, while the pore radius corresponding to each pore type was determined based on the quantitative analysis and combined with SEM and thin sections analysis, as detailed in Section 5.1); DT10, well ML1, 3554.1 m. (Q = quartz; F = feldspar; Do = dolomite; Ca = calcite; OM = organic matter.)

5.2. Significance of fractal dimension

The roughness and irregularity of the pore surface could be reflected by the fractal dimension. For the last few years, although some scholars have found that the fractal dimension of some coal and tight sandstones with more microfractures may be > 3.0 (Friesen and Mikula, 1987; Li and Horne, 2003; Li, 2010; Lai et al., 2015), the part of the > 3.0 is mainly used to describe the existence of microfractures (Li and Horne, 2003; Li, 2010; Lai et al., 2015). For the moment, the maximum value 3 of the fractal dimension indicates a completely irregular or rough surface, and the minimum value 2 represents a completely smooth surface (Giri et al., 2012; Gao et al., 2014; Lai et al., 2015). The fractal dimension could be used to evaluate many aspects of the pore structure, including factors such as pore throat size, connectivity, and pore size distribution (Sakhaee-Pour and Li, 2016; Fan et al., 2019). In NMR tests, $T_{2cutoff}$ value could reflect the proportion of large pores (movable fluid pores) in the rock, i.e., the higher the $T_{2cutoff}$ value, the larger the pores (movable fluid pores). Conversely, the lower the $T_{2cutoff}$ value, the smaller the pores (bound fluid pores). However, the pore structure information reflected by the fractal dimension is more comprehensive than the $T_{2cutoff}$ value, and it is a more effective index to characterize the pore structure (Shao et al., 2017).

Through analysis, it was found that there is a very significant negative correlation between D_2 and movable fluid porosity ($R^2 = 0.82$) (Fig. 18 A). Meanwhile, the relationship between the $T_{2cutoff}$ value and movable fluid porosity is not significant (Fig. 18 B), which is consistent with the previous studies (Shao et al., 2017; Fan et al., 2019), indicating that the information reflected by the $T_{2cutoff}$ value is not as comprehensive as that conveyed by the D_2. Although the permeability in the study area was low, even < 0.005 mD in some regions, it was still found that there is a clear negative correlation between D_2 and permeability ($R^2 = 0.57$) (Fig. 18 C). Samples deviating from the point of permeability and D_2 trend line tend to have more microfractures, leading to higher permeability (Fig. 18 C); otherwise, the correlation would be more obvious, which is in agreement with the results of Yang et al. (2016). According to the fractal theory and the fractal characteristics of rock pore network, fractal dimension is a comprehensive index reflecting the complexity of pore structure, including pore throat size, connectivity, pore size distribution, and other microscopic structure information (Shao et al., 2017; Fan et al., 2019). Therefore, the complexity of movable fluid pores could be directly characterized by D_2. In addition, based on the analysis in Section 5.1, the pore structure of the mixed fine-grained sedimentary rocks in the study area could be divided into four categories based on the NMR and HPMI results (Fig. 9). As the pore structure becomes more complex, the connectivity between pores and the regularity of pore surfaces gradually worsen (Figs. 14 and 16).

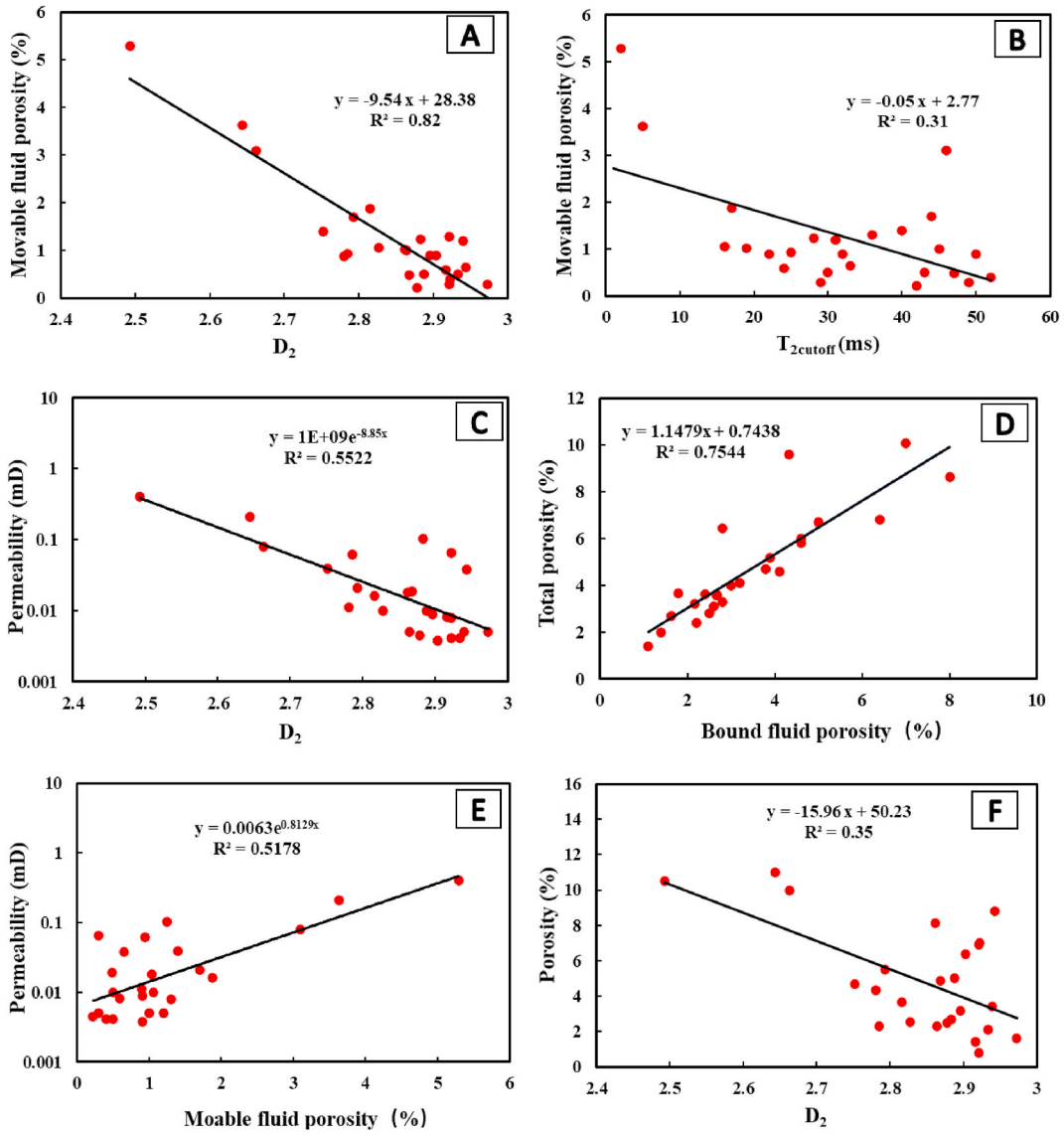

Fig. 18. Cross plots of fractal dimensions versus physical properties. (A) D_2 versus movable fluids porosity; (B) $T_{2cutoff}$ versus movable fluids porosity; (C) D_2 versus permeability; (D) Bound fluid porosity versus total NMR porosity; (E) Movable fluids porosity versus permeability; (F) D_2 versus porosity.

What's more, fluid flows easily in pores of regular shape and smooth surface, especially in large pore spaces. Therefore, fractal dimension could be used to evaluate the properties of reservoir fluids. Overall, D_2 is a comprehensive display of the complexity of pore structure, the higher the D_2 value, the more complicated the pore structure, the weaker the fluid mobility, the weaker the permeability, and the worse the connectivity of pores.

Fig. 18 D revealed that the total NMR porosity increases with increasing bound fluid porosity, and this correlation was more obvious than that between the total NMR porosity and movable fluid porosity, indicating that the proportion of small pores (bound fluid pores) in the study area was larger. Microscopic observations revealed that the large pores were mainly secondary pores formed by dissolution, devitrification, and dolomitization in the later period, especially in the dolomite reservoir (Fig. 14). In addition, a positive correlation between permeability and movable fluid porosity was found (Fig. 18 E), indicating that the fluid flow capacity was closely related to the permeability. Conversely, the D_2 and porosity have a relatively weak negative correlation (Fig. 18 F), which is similar to the previous research results. Although most of the previous studies were on tight sandstone, but the principle was similar. A lot of studies have proved that the correlation between D_2 and porosity of conventional sandstone reservoirs is often not obvious, because the porosity of sandstone is affected by the number of pores, especially the large pores rather than the complexity of the pore distribution (Li et al., 2016; Liang et al., 2015; Shao et al., 2017). For tight sandstones with a large number of small pores, however, the irregular distribution of small pores may restrict the development of large pores, thereby reducing the total porosity and mobile fluid porosity (Li et al., 2016; Shao et al., 2017; Fan et al., 2019). In the study area, the particle size of the mixed fine-grained sedimentary rocks was fine (<0.1 mm). Furthermore, inside the large pores, many materials such as authigenic quartz and OM were widespread, causing the large pores to become small-scale pores (Fig. 15), thereby reducing the total porosity and the mobile fluid porosity. Therefore, compared with the related parameters of NMR experiments, the fractal dimension is a more comprehensive index for characterizing and evaluating the pore structure.

5.3. *Effect of tuffaceous material and other minerals on fractal dimension*

Previous researchers have put a great deal of effort into examining the relationship between different mineral types and fractal dimension,

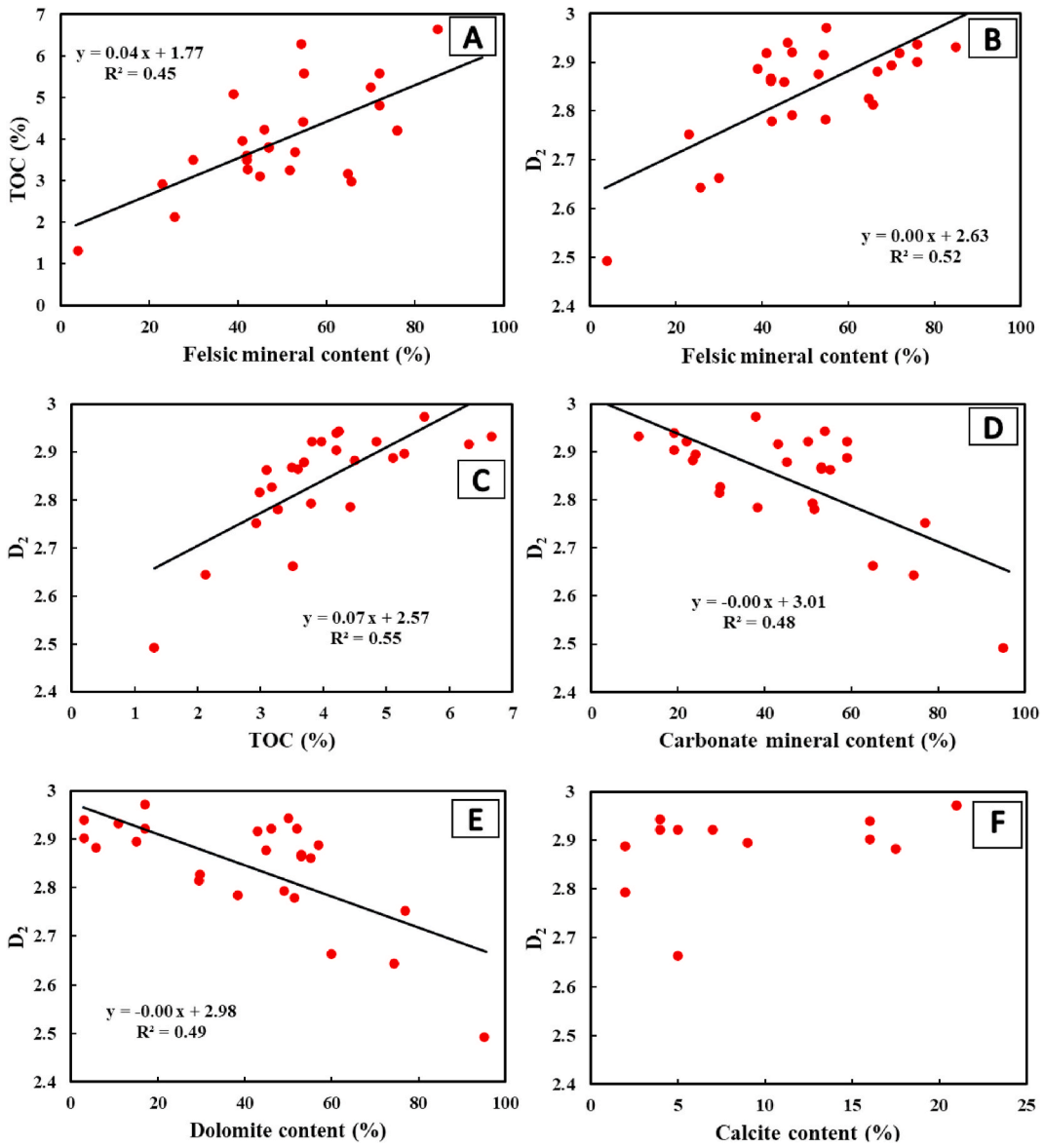

Fig. 19. Cross plots of fractal dimension versus mineral compositions. (A) Felsic mineral content versus TOC; (B) D_2 versus felsic mineral content; (C) D_2 versus TOC; (D) D_2 versus carbonate mineral content; (E) D_2 versus dolomite content; (F) D_2 versus calcite content.

and have confirmed that different mineral compositions have different effects on fractal dimension. In fact, even the same mineral has been found to exert different effects on fractal dimension in different genetic conditions (Shao et al., 2017; Lai et al., 2017; Wang et al., 2018; Fan et al., 2019). For example, Shao et al. (2017) and Fan et al. (2019) found that the quartz of different origin may have different effects on fractal dimension. Most of the sedimentary quartz grains play the role of framework mineral in tight sandstone, but some samples have high content of authigenic quartz crystals, leading to irregular pore shape and thus larger D_2 values. Wang et al. (2018) and Fan et al. (2019) argued that higher content of clay mineral would produce adverse effect on fractal dimension, but they had different opinions on the effect of the change of dolomite content on the fractal dimension. The former believed that the presence of dolomite as cement would have an adverse effect on the fractal dimension, while the latter found that the increase of dolomite content would have a favorable effect on the fractal dimension due to dissolution. However, there are few reports on the effect of volcanic ash on fractal dimension. A clear positive correlation among the tuffaceous material (felsic mineral) content, TOC content, and D_2 value can be seen in Fig. 19 Ã C, indicating that the pore structure becomes more irregular as the content of tuffaceous material increases. The volcanic ash falling into the lake encouraged algae to bloom and led to a great abundance of OM (Nishiyama et al., 2001; Li et al., 2014; Rakocinski et al., 2018; Ding et al., 2019), which could also block the intergranular pores of feldspar minerals (Fig. 16 Ã E) and even affect the dolomite intercrystal pores adjacent to the tuffaceous material (Fig. 16 F). This is consistent with the obvious negative correlation between the D_2 and permeability, i.e., when many of pores are blocked by OM, this may reduce the fluid mobility due to the adsorption by the OM, resulting in poor permeability and complex pore structure.

The volcanic ash sedimentation at the centimeter scale caused the lithology of the P_2l^2 to be complicated, and the dolomite even contained a small amount of tuffaceous material. Statistics revealed that the dolomite content has a significant negative correlation with the D_2 value (Fig. 19 D ~ E), which was due to the extensive dolomitization and dissolution processes that formed a large number of intercrystal pores and intercrystal dissolution pores, and even large-scale pores. As a result, the pore structure becomes more regular and geometrically simpler. The relationship between D_2 value and calcite content is not obvious (Fig. 19 F), which shows that the effect of calcite content on the

pore structure is not significant. It may be because the calcite content is less and even not developed. Although many studies have suggested that the clay minerals tend to increase the complexity of pore structure (Shao et al., 2017; Fan et al., 2019; Wang et al., 2018), the content of them in the study area is so low that the effect on the pore structure is negligible.

In general, the D_2 value increases with the increase of tuffaceous material (felsic mineral) content, and decreases with the increase of carbonate mineral content, i.e., the higher the dolomite content, the better the pore structure of the reservoir, and the simpler the geometry of the pores. On the contrary, the higher the tuffaceous material content, the worse the pore structure, and the more complicated the geometry of the pores.

6. Conclusions

(1) The mixed fine-grained sedimentary rock reservoir in the P_2l^2 is mainly composed of dolomite and felsic minerals, containing a small amount of calcite, clay, pyrite, and gypsum. The petrophysical properties of the reservoir are poor, and the pore systems are mainly composed of intergranular pores, intercrystal pores, intracrystal pores, intergranular dissolution pores, intercrystal dissolution pores, vugs, and microfractures.

(2) The NMR T_2 spectra of the dolomite reservoir are mainly dominated by the right unimodal type (1–100 ms), and the types of storage space are mainly intercrystal dissolution pores and intercrystal pores. A portion of the large T_2 components (>100 ms) represents microfractures and vugs, with low entry pressure. The NMR T_2 spectra of the tuff and transitional lithology reservoirs exhibit various morphologies, with the low T_2 components (0.01–1 ms) mostly representing intracrystal pores and intergranular pores blocked by OM, with high entry pressure and extreme heterogeneity of pore structure.

(3) The fractal dimension could be divided into two distinct segments based on the $T_{2cutoff}$ value measured by the NMR experiment, and the fractal theory is not applicable to the evaluation of the pore structure of the bound fluid pores ($T_2 < T_{2cutoff}$). However, for movable fluid pores ($T_2 > T_{2cutoff}$), the fractal dimension is an effective parameter to reflect the complexity of pore structure.

(4) Different mineral compositions and contents have different effects on the fractal results of reservoir pore structure. The D_2 value was found to decrease with increasing dolomite content and decreasing tuffaceous material (felsic mineral) content. The influence of calcite content on D_2 is not obvious, and the influence of clay mineral content on fractal dimension is negligible.

Declaration of competing interest

The authors declare that they have no known competing financial interests or personal relationships that could have appeared to influence the work reported in this paper.

Acknowledgments

This study was supported by State Key Laboratory of Petroleum Resources and Prospecting, China University of Petroleum (Beijing) and Accumulation and Development of Unconventional Oil and Gas, State Key Laboratory Cultivation Base Jointly-constructed by Heilongjiang Province and Ministry of Science and Technology, Northeast Petroleum University. And thanks to the National Natural Science Foundation of China (No.41702127). The authors acknowledge PetroChina Tuha Oilfield Company for providing data and data access for permission to publish this work.

Appendix A. Supplementary data

Supplementary data to this article can be found online at https://doi.org/10.1016/j.petrol.2021.108545.

Credit author statement

Yongshuai Pan: Experiments, Software, Investigation, Writing – original draft; Zhilong Huang: Conceptualization, Methodology; Tianjun Li: Samples, Writing – review & editing; Xiongfei Xu: Supervision; Writing – review & editing; Xuan Chen: Writing – review & editing; Xiaobo Guo: Writing – review & editing.

References

Aboud, M., Badry, R., Grau, J., Herron, S., Hamichi, F., Horkowitz, J., Hemingway, J., MacDonald, R., Saldungaray, P., Stachiw, D., 2014. High-definition spectroscopy: determining mineralogic complexity. Oilfield Rev. 26, 34–50.

Brandano, M., Civitelli, G., 2007. Non-seagrass meadow sedimentary facies of the Pontinian Islands, Tyrrhenian Sea: a modern example of mixed carbonate-siliciclastic sedimentation. Sediment. Geol. 201 (3–4), 286–301.

Bai, B., Zhu, R.K., Wu, S.T., Yang, W.J., Gelb, J., Gu, A., Zhang, X.X., Su, L., 2013. Multi-scale method of nano(micro)-CT study on microscopic pore structure of tight sandstone of Yanchang Formation, Ordos Basin. Petrol. Explor. Dev. 40 (3), 329–333.

Cózar, P., Somerville, I.D., Rodríguez, S., Mas, R., Medina-Varea, P., 2006. Development of a late Viséan (Mississippian) mixed carbonate/siliciclastic platform in the Guadalmellato Valley (southwestern Spain). Sediment. Geol. 183, 269–295.

Choquette, P.A., Pray, L.C., 1970. Geologic nomenclature and classification of porosity in sedimentary carbonates. AAPG Bull. 54 (2), 207–250.

Clarkson, C.R., Solano, N., Bustin, R.M., Bustin, A., Chalmers, G., He, L., Melnichenko, Y. B., Radliński, A., Blach, T.P., 2013. Pore structure characterization of North American shale gas reservoirs using USANS/SANS, gas adsorption, and mercury intrusion. Fuel 103, 606–616.

Deng, Y., Pu, X.G., Chen, S.Y., Yan, J.H., Shi, Z.N., Zhang, W., Han, W.Z., 2019. Characteristics and controlling factors of fine-grained mixed sedimentary rocks reservoir: a case study of the 2nd member of Kongdian Formation in Cangdong depression, Bohai Bay basin. J. China Inst. Min. Technol. 48 (6), 1301–1316.

Desbois, G., Janos, L.U., Kukla, P.A., Konstanty, J., Baerle, C., 2011. High-resolution 3D fabric and porosity model in a tight gas sandstone reservoir: a new approach to investigate microstructures from mm- to nm-scale combining argon beam cross-sectioning and SEM imaging. J. Petrol. Sci. Eng. 78 (2), 243–257.

Dillinger, A., Esteban, L., 2014. Experimental evaluation of reservoir quality in Mesozoic formations of the Perth Basin (Western Australia) by using a laboratory low field Nuclear Magnetic Resonance. Mar. Petrol. Geol. 57, 455–469.

Edahbi, M., Benzaazoua, M., Plante, B., Doire, S., Kormos, L., 2017. Mineralogical characterization using QEMSCAN? and leaching potential study of REE within silicate ores: a case study of the Matamec project, Québec, Canada. J. Geochem. Explor. 185, 64–73.

Friesen, W.I., Mikula, R.J., 1987. Fractal dimensions of coal particles. J. Colloid Interface Sci. 120 (1), 263–271.

Fu, X.D., Wu, J.P., Shou, J.F., Wang, X.F., Zhou, J.G., Zhang, T.F., Guo, Y.J., 2019. Tight oil reservoir characteristics of lacustrine mixed marlstone in the Palaeogene Shahejie Formation of Shulu sag, Bohai Bay Basin. Oil Gas Geol. 40 (1), 82–95.

Fan, X.Q., Wang, G.W., Li, Y.F., Dai, Q.Q., Linghu, S., Duan, C.W., Zhang, C.E., Zhang, F. S., 2019. Pore structure evaluation of tight reservoirs in the mixed siliciclastic-carbonate sediments using fractal analysis of NMR experiments and logs. Mar. Petrol. Geol. 109, 484–493.

Guan, M., Liu, X.P., Jin, Z.J., Lai, J., 2020. The heterogeneity of pore structure in lacustrine shales: insights from multifractal analysis using N2 adsorption and mercury intrusion. Mar. Petrol. Geol. 114, 104150.

Giffin, S., Littke, R., Klaver, J., Urai, J.L., 2013. Application of BIB-SEM technology to characterize macropore morphology in coal. Int. J. Coal Geol. 114, 85–95.

Giri, A., Tarafdar, S., Gouze, P., Dutta, T., 2012. Fractal pore structure of sedimentary rocks: simulation in 2-D using a relaxed bidisperse ballistic deposition model. J. Appl. Geophys. 87 (12), 40–45.

Gao, H.J., Yu, B.M., Duan, Y.G., Fang, Q.T., 2014. Fractal analysis of dimensionless capillary pressure function. Int. J. Heat Mass Tran. 69, 26–33.

Ge, X.M., Fan, Y.R., Zhu, X.J., Chen, Y.G., Li, R.Z., 2014. Determination of nuclear magnetic resonance T2 cutoff value based on multifractal theory—an application in sandstone with complex pore structure. Geophysics 80, D11–D21.

Jarvie, D.M., 2010. Unconventional oil petroleum systems: shales and shale hybrids. In: AAPG Conference and Exhibition. Calgary, Alberta, Canada, September, pp. 12–15.

Jia, C.Z., Zheng, M., Zhang, Y.F., 2012. Unconventional hydrocarbon resources in China and the prospect of exploration and development. Petrol. Explor. Dev. 39 (2), 139–146.

Kulesza, S., Bramowicz, M., 2014. A comparative study of correlation methods for determination of fractal parameters in surface characterization. Appl. Surf. Sci. 293 (8), 196–201.

Katz, A.J., Thompson, A.H., 1985. Fractal sandstone pores: implications for conductivity and pore formation. Phys. Rev. Lett. 54 (12), 1325–1328.

Kumar, S., Mendhe, V.A., Kamble A, D., Varma, A.K., Mishra, D.K., Bannerjee, M., Buragohain, J., Prasad, A.K., 2019. Geochemical attributes, pore structures and fractal characteristics of Barakar shale deposits of Mand-Raigarh Basin, India. Mar. Petrol. Geol. 103, 377–396.

Klaver, J., Desbois, G., Littke, R., Urai, J.L., 2015. BIB-SEM characterization of pore space morphology and distribution in postmature to overmature samples from the Haynesville and Bossier Shales. Mar. Petrol. Geol. 59, 451–466.
Lai, J., Wang, S., Zhang, C.S., Wang, G.W., Song, Q.Q., Chen, X., Yang, K.F., Yuan, C.J., 2020. Spectrum of pore types and networks in the deep cambrian to lower ordovician dolostones in tarim basin, China. Mar. Petrol. Geol. 112, 104081.
Liu, X.F., Nie, B.S., 2016. Fractal characteristics of coal samples utilizing image analysis and gas adsorption. Fuel 182, 314–322.
Li, A., Ding, W.L., He, J.H., Dai, P., Yin, S., Xie, F., 2016. Investigation of pore structure and fractal characteristics of organic-rich shale reservoirs: a case study of Lower Cambrian Qiongzhusi formation in Malong block of eastern Yunnan Province, South China. Mar. Petrol. Geol. 70, 46–57.
Li, K., 2010. Analytical derivation of Brooks-Corey type capillary pressure models using fractal geometry and evaluation of rock heterogeneity. J. Petrol. Sci. Eng. 73, 20–26.
Li, Z., Wu, S.H., Xia, D.L., He, S.C., Zhang, X.F., 2018. An investigation into pore structure and petrophysical property in tight sandstones: a case of the Yanchang Formation in the southern Ordos Basin, China. Mar. Petrol. Geol. 97, 390–406.
Lai, J., Wang, G.W., Wang, Z.Y., Chen, J., Pang, X.J., Wang, S.C., Zhou, Z.L., He, Z.B., Qin, Z.Q., Fan, X.Q., 2017. A review on pore structure characterization in tight sandstones. Earth Sci. Rev. 177, 436–457.
Lin, B.T., Chen, M., Jin, Y., Pang, H.W., 2015. Modeling pore size distribution of southern Sichuan shale gas reservoirs. J. Nat. Gas Sci. Eng. 26, 883–894.
Lai, J., Wang, G.W., 2015. Fractal analysis of tight gas sandstones using high-pressure mercury intrusion techniques. J. Nat. Gas Sci. Eng. 24, 185–196.
Liu, B., Lü, Y.F., Zhao, R., Tu, X.X., Guo, X.B., Shen, Y., 2012. Formation overpressure and shale oil enrichment in the shale system of Lucaogou Formation, Malang sag, Santanghu Basin. NW Petroleum Exploration and Development 39, 744–750.
Liu, B., Lü, Y.F., Meng, Y.L., Li, X.N., Guo, X.B., Ma, Q., Zhao, W.C., 2015. Petrologic characteristics and genetic model of lacustrine lamellar fine-grained rock and its significance for shale oil exploration: a case study of Permian Lucaogou Formation in Malang sag, Santanghu Basin, NW China. Petrol. Explor. Dev. 42 (5), 656–666.
Liu, B., Bechtel, A., Sachsenhofer, R.F., Gross, D., Gratzer, R., Chen, X., 2017. Depositional environment of oil shale within the second member of permian Lucaogou Formation in the Santanghu Basin, northwest China. Int. J. Coal Geol. 175, 10–25.
Liu, G.H., Zhai, G.Y., Huang, Z.L., Zou, C.N., Xia, X.H., Shi, D.S., Zhou, Z., Zhang, C., Chen, R., Yu, S.F., Chen, L., Zhang, S.H., 2019. The effect of tuffaceous material on characteristics of different lithofacies: a case study on Lucaogou Formation fine-grained sedimentary rocks in Santanghu Basin. J. Petrol. Sci. Eng. 179, 355–377.
Li, T.J., Huang, Z.L., Feng, Y., Chen, X., Ma, Q., Liu, B., Guo, X.B., 2020. Reservoir characteristics and evaluation of fluid mobility in organic-rich mixed siliciclastic-carbonate sediments: a case study of the lacustrine Qiketai Formation in Shengbei Sag, Turpan-Hami Basin, Northwest China. J. Petrol. Sci. Eng. 185, 920–4105.
Li, A.F., Ren, X.X., Wang, G.J., Wang, Y.Z., Jiang, K.L., 2015. Characterization of pore structure of low permeability reservoirs using an uclear magnetic resonance method. Journal of China University of Petroleum (Edition of Natural Science) 39 (6), 92–98.
Li, K.W., Horne, R.N., 2003. Fractal Characterization of the geysers rock. Trans. Geotherm. Resour. Counc. 27, 1–8.
Li, D.H., Li, J.Z., Huang, J.L., Wang, S.Y., Wang, S.F., 2014. An important role of volcanic ash in the formation of shale plays and its inspiration. Nat. Gas. Ind. 34 (5), 56–65.
Liang, L.X., Xiong, J., Liu, X.J., 2015. An investigation of the fractal characteristics of the Upper Ordovician Wufeng Formation shale using nitrogen adsorption analysis. J. Nat. Gas Sci. Eng. 27, 2–409.
McNeill, D.F., Klaus, J.S., Budd, A.F., Lutz, B.P., Ishman, S.E., 2012. Late Neogene chronology and sequence stratigraphy of mixed carbonate-siliciclastic deposits of the Cibao Basin, Dominican Republic. Geol. Soc. Am. Bull. 124, 35–58.
Mohammadi, E., Hasanzadeh-Dastgerdi, M., Safari, A., Moghaddam, H.V., 2018. Microfacies and depositional environments of the Qom Formation in Barzok area, SW Kashan, Iran. Carbonates Evaporites 34, 1293–1306.
Mount, J., 1984. Mixing of siliciclastic and carbonate sediments in shallow shelf environments. Geology 7, 432–435.
Mandelbrot, B.B., 1977. The Fractal Geometry of Nature. W. Freeman, New York.
Ma, X., Guo, S.B., Shi, D.S., Zhou, Z., Liu, G.H., 2019. Investigation of pore structure and fractal characteristics of marine-continental transitional shales from Longtan Formation using MICP, gas adsorption, and NMR (Guizhou, China). Mar. Petrol. Geol. 107, 555–571.
Ma, J., Huang, Z.L., Liang, S.J., Liu, Z.Z., Liang, H., 2016. Geochemical and tight reservoir characteristics of sedimentary organic-matter-bearing tuff from the permian Tiaohu Formation in the Santanghu Basin, northwest China. Mar. Petrol. Geol. 73, 405–418.
Müller-Huber, E., Schön, J., Börner, F., 2016. Pore space characterization in carbonate rocks- approach to combine nuclear magnetic resonance and elastic wave velocity measurements. J. Appl. Geophys. 127, 68–81.
Nabawy, B.S., David, C., 2016. X-ray CT scanning imaging for the Nubia sandstone as a tool for characterizing its capillary properties. Geosci. J. 20 (5), 1–14.
Nishiyama, M., Sumikawa, Y., Guan, G., Marumoto, T., 2001. Relationship between microbial biomass and extractable organic carbon content in volcanic and non-volcanic ash soil. Appl. Soil Ecol. 17 (2), 187.
Pan, Y.S., Huang, Z.L., Li, T.J., Guo, X.B., Xu, X.F., Chen, X., 2020. Environmental response to volcanic activity and its effect on organic matter enrichment in the permian Lucaogou Formation of the Malang sag, Santanghu Basin, northwest China. Palaeogeogr. Palaeoclimatol. Palaeoecol. 560, 110024.
Qi, Y.M., Zhang, S.L., Wu, J.Y., Lv, Z.X., 2019. Diagenesis characteristics of Shahejie Formation deep-Buried mixed siliciclastic-carbonate sediments in the Shijiutuo uplift, Bohai Sea. Geol. Sci. Technol. Inf. 38 (3), 69–75.
Rietveld, H.M., 1969. A profile refinement method for nuclear and magnetic structures. J. Appl. Crystallogr. 2, 65–71.
Rakocinski, M., Zaton, M., Marynowski, L., Gedl, P., Lehmann, J., 2018. Redox conditions, productivity, and volcanic input during deposition of uppermost Jurassic and Lower Cretaceous organic-rich siltstones in Spitsbergen, Norway. Cretac. Res. 89, 126–147.
Sakhaee-Pour, A., Bryant, S.L., 2014. Effect of pore structure on the producibility of tight-gas sandstones. AAPG Bull. 98, 663–694.
Sakhaee-Pour, A., Bryant, S.L., 2015. Pore structure of shale. Fuel 143, 467–475.
Sakhaee-Pour, A., Li, W.F., 2016. Fractal dimensions of shale. J. Nat. Gas Sci. Eng. 30, 578–582.
Sakhaee-Pour, A., 2017. Decomposing J-function to account for the pore structure effect in tight gas sandstones. Transport Porous Media 116 (2), 453–471.
Shan, C.G., Zhao, W.W., Wang, F.Q., Zhang, K., Feng, Z., Guo, L.L.B., Ma, X.L., Liao, T., 2020. Nanoscale pore structure heterogeneity and its quantitative characterization in Chang7 lacustrine shale of the southeastern Ordos Basin, China. J. Petrol. Sci. Eng. 187, 106754.
Song, S.B., Liu, J.F., Yang, D.S., Ni, H.Y., Huang, B.X., Zhang, K., Mao, X.B., 2019a. Pore structure characterization and permeability prediction of coal samples based on SEM images. J. Nat. Gas Sci. Eng. 67, 160–171.
Shao, X.H., Pang, X.Q., Li, H., Zhang, X., 2017. Fractal analysis of pore network in tight gas sandstones using NMR method: a case study from the Ordos Basin, China. Energy Fuels 31, 10358–10368.
Song, L., Martin, K., Carr, T., Ghahfarokhi, P., 2019b. Porosity and storage capacity of Middle Devonian shale: a function of thermal maturity, total organic carbon, and clay content. Fuel 241, 1036–1044.
Timur, A., Hempkins, W., Weinbrandt, R., 1971. Scanning electron microscope study of pore systems in rocks. Journal of Geophysical Research Atmospheres 76, 4932–4948.
Testamanti, M.N., Rezaee, R., 2017. Determination of NMR T2cut-off for clay bound water in shales: a case study of Carynginia Formation, Perth Basin, Western Australia. J. Petrol. Sci. Eng. 149, 497–503.
Wang, H., Shi, Y.M., Xu, D.W., Chen, X., Li, L.M.C.D., 2019. Unconventional reservoir pore structure characterization techniques and progress. Petroleum Geology and Recovery Efficiency 26 (5), 21–30.
Wang, Q.C., Chen, D.X., Gao, X.Z., Wang, F.W., Li, J.H., Liao, W.H., Wang, Z.Y., Xie, G.J., 2020. Microscopic pore structures of tight sandstone reservoirs and their diagenetic controls: a case study of the Upper Triassic Xujiahe Formation of the Western Sichuan Depression, China. Mar. Petrol. Geol. 113, 104119.
Wei, W., Zhu, X.M., Azmy, K., Zhu, S.F., He, M.W., Sun, S.Y., 2020. Depositional and compositional controls on diagenesis of the mixed siliciclastic-volcaniclastic sandstones: a case study of the Lower Cretaceous in Erennaoer Sag, Erlian Basin, NE China. J. Petrol. Sci. Eng. 188, 106855.
Wang, Z.Y., Pan, M., Shi, Y.M., Liu, L., Xiong, F.Y., Qin, Z.Q., 2018. Fractal analysis of Donghetang sandstones using NMR measurements. Energy Fuel. 32, 2973–2982.
Xi, K.L., Cao, Y.C., Haile, B.G., Zhu, R.K., Jahren, J., Bjørlykke, K., Zhang, X.X., Hellevang, H., 2016. How does the pore-throat size control the reservoir quality and oiliness of tight sandstones? The case of the Lower Cretaceous Quantou Formation in the southern Songliao Basin, China. Mar. Petrol. Geol. 76, 1–15.
Xu, Z.P., Lin, M., Jiang, W.B., Cao, G.H., Yi, Z.X., 2020. Identifying the comprehensive pore structure characteristics of a rock from 3D images. J. Petrol. Sci. Eng. 187, 106764.
Xu, H., Tang, D.Z., Zhang, J.F., 2013. Coexistence mechanism of multi-types of reservoir pressure in the Malang depression of the Santanghu Basin, China. J. Petrol. Sci. Eng. 108, 279–287.
Yang, F., Ning, Z.F., Liu, H.Q., 2016. Fractal characteristics of shales from a shale gas reservoir in the Sichuan Basin, China. Fuel 115 (1), 378–384.
Yu, C., Tran, H., Sakhaee-Pour, A., 2018. Pore size of shale based on acyclic pore model. Transport Porous Media 124, 345–368.
Zhang, S.M., Cao, Y.C., Liu, K.Y., Jahren, J., Xi, K.L., Zhu, R.K., Yang, T., Cao, X., Wang, W., 2019. Characterization of lacustrine mixed fine-grained sedimentary rocks using coupled chemostratigraphic-petrographic analysis: a case study from a tight oil reservoir in the Jimusar Sag, Junggar Basin. Mar. Petrol. Geol. 99, 453–472.
Zhang, Z.J., Liu, S.G., Zhang, C.J., Xu, G.S., 2007. Reservoir characteristics of Qom Formation in Kashan area, the central Iranian basin. West China Petroleum Geosciences 3, 62–68.
Zhang, L.C., Lu, S.F., Xiao, D.S., Li, B., 2017. Pore structure characteristics of tight sandstones in the northern Songliao Basin, China. Mar. Petrol. Geol. 88, 170–180.
Zhou, L., Kang, Z.H., 2016. Fractal characterization of pores in shales using NMR: a case study from the lower cambrian niutitang Formation in the middle Yangtze platform, southwest China. J. Nat. Gas Sci. Eng. 35, 860–872.
Zhang, Z.Y., Weller, A., 2014. Fractal dimension of pore-space geometry of an Eocene sandstone formation. Geophysics 79, 377–387.
Zhou, S.D., Liu, D.M., Cai, Y.D., Yao, Y.B., Che, Y., Liu, Z.H., 2017. Multi-scale fractal characterizations of lignite, subbituminous and high-volatile bituminous coals pores by mercury intrusion porosimetry. J. Nat. Gas Sci. Eng. 44, 338–350.
Zhao, P.Q., Wang, Z.L., Sun, Z.C., Cai, J.C., Wang, L., 2017. Investigation on the pore structure and multifractal characteristics of tight oil reservoirs using NMR measurements: Permian Lucaogou Formation in Jimusaer Sag, Junggar Basin. Mar. Petrol. Geol. 86, 1067–1081.
Zhou, D.W., Liu, Y.Q., Xing, X.J., Hao, J.R., Dong, Y.P., Ouyang, Z.J., 2006. Formation of the Permian basalts and implications of geochemical tracing for paleo-tectonic setting and regional tectonic background in the Turpan-Hami and Santanghu basins, Xinjiang. Sci. China Earth Sci. 49, 584–596.